Late Paleozoic tectonic evolution of the Paleo-Asian Ocean in the northern Alxa Block (NW China)

Guoai Xie[1], Rongsong Tian[1], Wenbin Zhu[1], Jin Zhang[2], Shuang Gao[3], Beihang Zhang[2], Heng Zhao[4], and Tian Li[3]

[1]School of Earth Sciences and Engineering, Nanjing University
[2]Key Laboratory of Deep-Earth Dynamics of Ministry of Natural Resources, Institute of Geology, Chinese Academy of Geological Sciences, Beijing, China
[3]State Key Laboratory for Mineral Deposits Research, School of Earth Sciences and Engineering, Nanjing University
[4]Key Laboratory of Deep-Earth Dynamics of Ministry of Natural Resources, Institute of Geology, Chinese Academy of Geological

November 26, 2022

Abstract

The northern Alxa Block occupies a key position in the southern margin of Central Asian Orogenic Belt (CAOB) and records late Paleozoic subduction and closure processes of the Paleo–Asian Ocean (PAO). However, there are still controversies regarding the timing and location of the final closure of the PAO. This study presents structural deformation data, geochronological and geochemical data for Permian volcanic rocks, as well as detrital zircon provenance analysis of Permian sedimentary rocks along the Nuoergong - Langshan Zone (NLZ) in the northern Alxa Block. During the Carboniferous to middle Permian, the Paleo-Asian Ocean (PAO) lithospheric slab subducts beneath the northern Alxa Block, rendering a continental volcanic arc in the NLZ and also giving rise to extensive folding, thrusting and crustal thickening. Subsequently, a retroarc foreland basin was developed behind the continental volcanic arc, where pyroclastic material with Carboniferous to Permian ages from the volcanic arc and sediments eroded from the Alxa Precambrian basements were deposited (Dahongshan Formation) during middle Permian (Ca. 261 Ma). A large-scale dextral ductile shear deformation in the NLZ resulting from the lateral extrusion of the thickened crust after the continental collision was constrained between 272 Ma and 249 Ma, suggesting a middle Permian tectonic transition from compression to transpression. Combining with published data, we suggest that the final consumption of the PAO occurred in the middle to late Permian, probably along the Qagan Qulu suture zone in the northern Alxa Block.

Late Paleozoic tectonic evolution of the Paleo-Asian Ocean in the northern Alxa Block (NW China)

Rongsong Tian[1], Guoai Xie[1]*, Wenbin Zhu[1]*, Jin Zhang[2], Shuang Gao[1], Beihang Zhang[2], Heng Zhao[2], Tian Li[1]

1. State Key Laboratory for Mineral Deposits Research, Institute of Continental Geodynamics, School of Earth Sciences and Engineering, Nanjing University, Nanjing, 210093, China; 2. Key Laboratory of Deep–Earth Dynamics of Ministry of Natural Resources, Institute of Geology, Chinese Academy of Geological Sciences, Beijing, 100037, China

Corresponding author, Tel.:+86 138518928465.

E-mail address: xganju@126.com (G. Xie); zwb@nju.edu.cn (W. Zhu)

Key points:

- Early – middle Permian continental volcanic arc was recognized in Nuoergong – Langshan Zone in the northern Alxa Block.
- Permian subduction and crustal thickening processes existed along the southern Central Asian Orogenic Belt (CAOB).
- Transcurrent dextral shear zone developed in the southern CAOB, probably resulting from the lateral extrusion of the thickened crust.

Abstract: The northern Alxa Block occupies a key position in the southern margin of

Central Asian Orogenic Belt (CAOB) and records late Paleozoic subduction and closure processes of the Paleo–Asian Ocean (PAO). However, there are still controversies regarding the timing and location of the final closure of the PAO. This study presents structural deformation data, geochronological and geochemical data for Permian volcanic rocks, as well as detrital zircon provenance analysis of Permian sedimentary rocks along the Nuoergong - Langshan Zone (NLZ) in the northern Alxa Block. During the Carboniferous to middle Permian, the Paleo-Asian Ocean (PAO) lithospheric slab subducts beneath the northern Alxa Block, rendering a continental volcanic arc in the NLZ and also giving rise to extensive folding, thrusting and crustal thickening. Subsequently, a retroarc foreland basin was developed behind the continental volcanic arc, where pyroclastic material with Carboniferous to Permian ages from the volcanic arc and sediments eroded from the Alxa Precambrian basements were deposited (Dahongshan Formation) during middle Permian (Ca. 261 Ma). A large-scale dextral ductile shear deformation in the NLZ resulting from the lateral extrusion of the thickened crust after the continental collision was constrained between 272 Ma and 249 Ma, suggesting a middle Permian tectonic transition from compression to transpression. Combining with published data, we suggest that the final consumption of the PAO occurred in the middle to late Permian, probably along the Qagan Qulu suture zone in the northern Alxa Block.

1. Introduction

The Central Asian Orogenic Belt (CAOB) has undergone long–lived evolution from the Neoproterozoic to the Triassic, forming one of the largest and most complex Phanerozoic accretionary orogenic systems on Earth (Fig. 1a) (Şengör et al., 1993, 2018; Windley et al., 2007; Xiao et al., 2013, 2015). The southernmost segment of the CAOB extends from the Tianshan and Beishan orogens in NW China to the Xing' an - Mongolian orogen in NE China and preserves the history of late Paleozoic to early Mesozoic closure of the Paleo–Asian Ocean (PAO) by subduction and subsequent continental collision with the Tarim and North China blocks (Han et al., 2011; Jian et al., 2010; Eizenhöfer and Zhao et al., 2018; Xiao et al., 2015). The northern margin of the Alxa Block occupies a key position in the middle segment of the southernmost CAOB (Fig. 1b) and connects the Beishan and Tianshan orogens to the west and the Xing' an - Mongolian orogen to the east.

The timing and location of the final closure of the PAO is crucial for our understanding of the tectonic evolution of the CAOB. Considerable progress on the tectonic evolution of the PAO has been made in the western and eastern segment of the CAOB (Jian et al., 2010; Eizenhöfer et al., 2014; Klemd et al., 2015; Zhang et al., 2015a, 2016a; Wang et al., 2018a) and several related tectonic evolution syntheses have recently been published (Han et al., 2011; Xiao et al., 2015, 2018; Eizenhöfer and Zhao et al., 2018). In the central segment of the CAOB, i.e., the northern margin of Alxa Block, extensive mapping, geochemical and geochronological work have been carried out in recent years (Dan et al., 2014a, b, 2015; Shi et al., 2014a, 2016; Hu et al., 2014; Gong et al., 2012, 2016; J. J. Zhang et al., 2015b, 2016b; Song et al., 2018a). These studies have established the major magmatic events, basement components and sedimentary records in the northern Alxa Block. However, there are still considerable disagreements regarding the time and location of the final closure of the PAO in this area. Some researchers suggested that the Engger Us ophiolite belt (Fig. 1b) represents the suture zone between the Alxa Block and the southern CAOB (Wu and He, 1993; Zheng et al., 2014), whereas others maintained that the Qagan Qulu ophiolite belt is the location of final closure of the PAO (Shi et al., 2014a, b; J. J. Zhang et al., 2015b). These disagreements primarily stem from different interpretations of tectonic settings during the late Carboniferous to Permian in the northern Alxa Block.

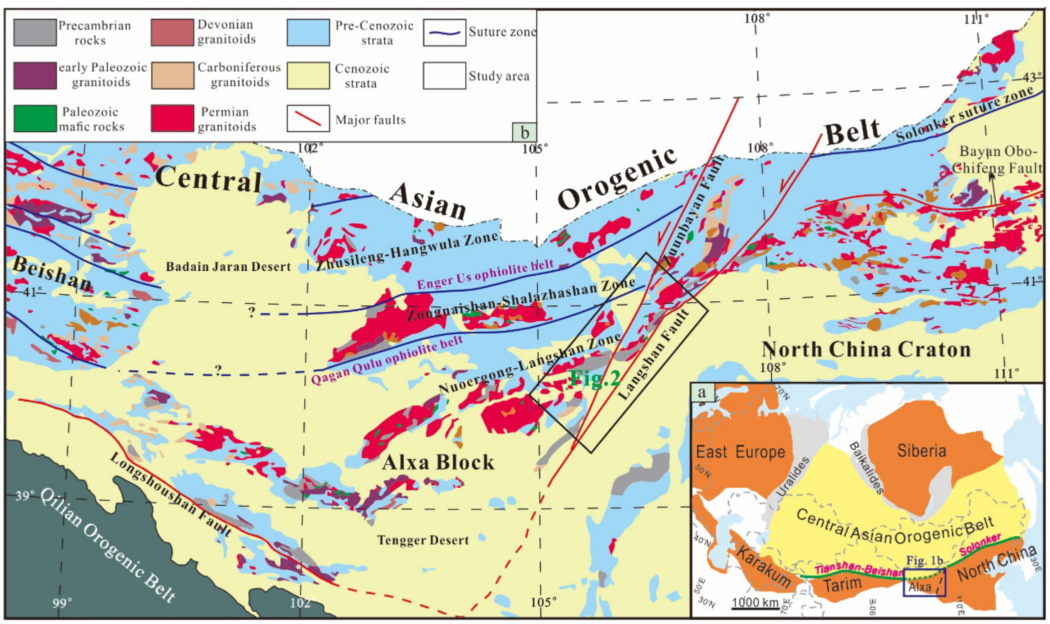

Figure 1. (a) Sketch map of the Central Asian Orogenic Belt showing the location of the Alxa Block. Modified from Xiao et al. (2015); (b) Schematic geological map of the Alxa Block and its adjacent areas, showing the distribution of magmatic rocks and major tectonic boundaries (Modified after Zhang et al. 2015b; Tian et al. 2019).

The timing of the final consumption of the PAO has also been disputed. Several authors suggested an early Permian extension related to a mantle plume (Dan et al., 2014b, 2015) or continental rifting (Zhang et al., 2012; Shi et al., 2018) in the northern Alxa Block, implying that the PAO has closed before the early Permian. However, many researchers proposed that there is a Carboniferous to middle Permian continental arc setting in this area (Feng et al., 2013; Peng et al., 2013; Yang et al., 2014; Liu et al., 2017a; Song et al., 2018a, b) and argued that the PAO was not consumed until the early to middle Permian. This controversy is mainly due to non-unique interpretations of isotopic and geochemical analyses of the Carboniferous to early Permian plutonic rocks.

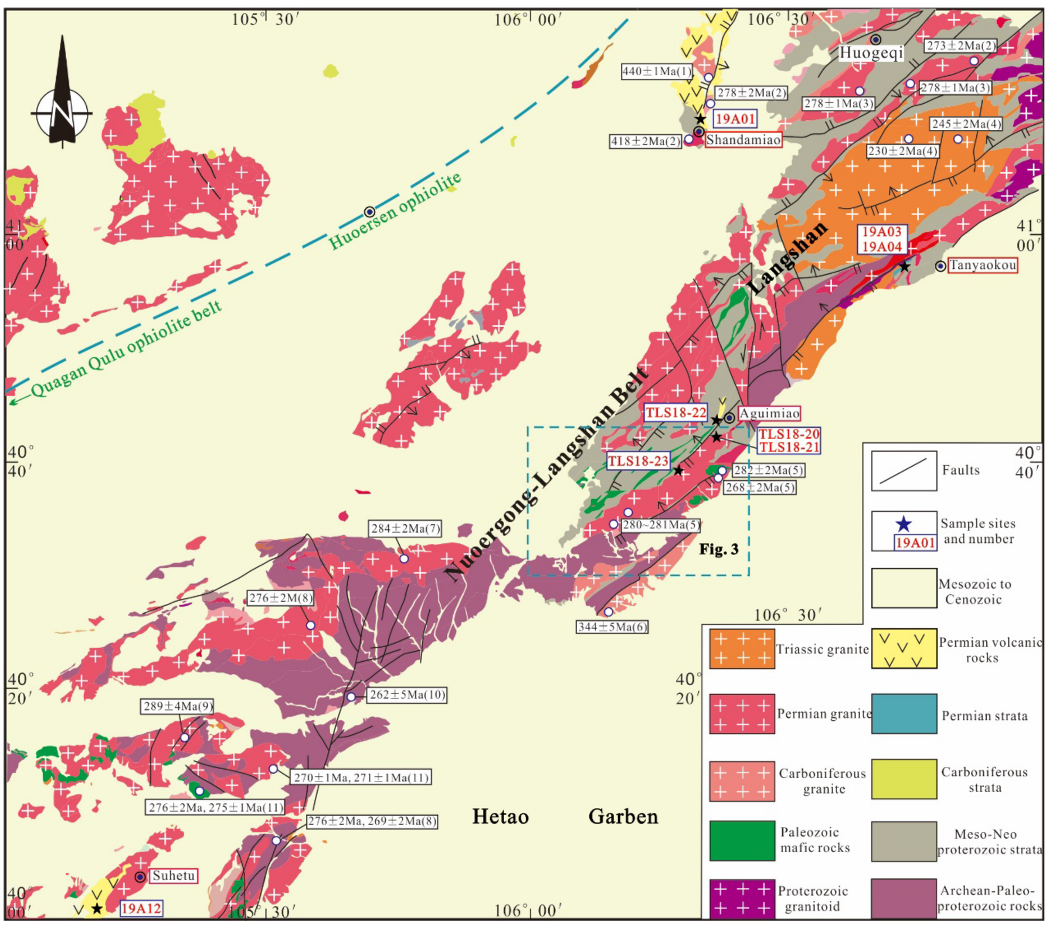

Figure 2. Geological map of the Langshan region showing the distribution of major lithostratigraphic units and sampling locations (modified after 1:200,000 geological maps from the Bureau of Geology and Mineral Resources of Inner Mongolia Autonomous Region (1991). References of geochronological data are listed in Appendix Table S3.

In this paper, we combine structural analysis, zircon U – Pb ages and geochemistry of Permian volcanic rocks, as well as detrital zircon provenance analysis of Permian strata, to interpret the late Paleozoic tectonic setting in the northern Alxa Block. Our data provide important constraints on the timing and nature of structural and magmatic events in the northern Alxa Block and contribute to establishing a more comprehensive model for the final evolution of the PAO in the southern CAOB.

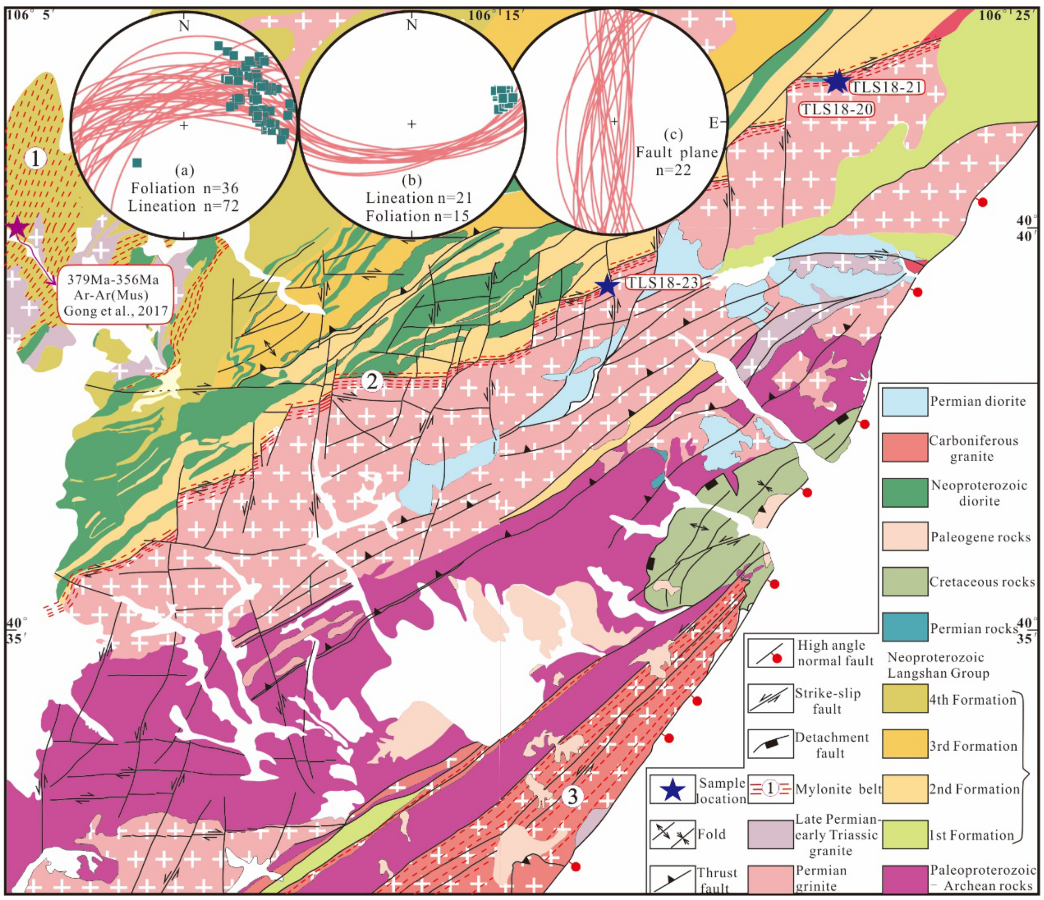

Figure 3. Detailed geological map in the study area showing major structural elements. Stereographic projections show (a) stretching lineations and foliations in granitic mylonites and felsic mylonites in the central and southwestern region, (b) stretching lineations (squares) and foliations in granitic mylonites in the northeastern region, and (c) nearly north–south trending fault planes (lower hemisphere, equal area).

2. Regional Tectonics

The Alxa Block is located in a key place that bridges the CAOB to the north, the Tarim Craton to the west and North China Craton to the east (Fig. 1a, b). The Alxa Block is separated by the NE–SW trending Langshan Fault from NCC and by the Longshoushan Fault from the early Paleozoic North Qilian Orogenic Belt. The western and southern parts of the Alxa Block are covered by Cenozoic sediments of the Badain Jaran Desert and Tengger Desert, respectively (Fig. 1b).

The Archean–Paleoproterozoic basement rocks occur in the Alxa Block and record similar magmatic–metamorphic events with those in the NCC, suggesting that the Alxa Block is the westernmost part of NCC, either as a part of the Khondalite Belt or the Yinshan Block (J. X. Zhang et al., 2013b; Gong et al., 2016). However, the discovery of Neoproterozoic S–type granite in the Alxa Block and the comparable early Paleozoic detrital zircon age spectra to the South China Craton suggest that the Alxa Block had probably separated from the NCC before the Neoproterozoic (Dan et al., 2014a; J. Zhang et al., 2015c). Despite this controversy, it generally accepted that the northern margins of the Alxa and North China have both experienced tectonic and magmatic events related to the evolution of the PAO and subsequent intracontinental deformation (Zhang et al., 2009a, b; Feng et al., 2013; Wang and Wan. 2014; Liu et al., 2016a).

In the northern Alxa Block, two major faults, i.e., the Engger Us Fault and the Quagan Qulu Fault, divide the block into, from north to south, the Zhusileng – Hangwula, Zongnaishan – Shalazhashan and Nuoergong – Langshan zones (Fig. 1b). The Zhusileng – Hangwula Zone (ZHZ) is thought to be the middle part of the southernmost CAOB that extends eastward into Mongolia and is covered by the Badain Jaran Desert to the west. Neoproterozoic metasedimentary rocks are sporadically exposed, including marble, quartzite, sandstone, and phyllite (BGMRNM, 1991). Minor granitic gneisses with U–Pb ages of 916Ma and 905Ma were also reported in this zone (Wang et al., 2001; Zhou et al., 2013), indicating a microcontinent with Precambrian basement. During the early Paleozoic, this zone was devoid of volcanic sediments but received a succession of clastic sediments, implying a passive continental margin (Wu and He. 1993). By contrast, late Paleozoic sedimentary sequences are widely distributed in this area and dominantly consist of deep-sea flysh associated with volcanic sediments (BGMRNM, 1991). Late Ordovician (453Ma) and Carboniferous to Permian granitoids (313~277Ma) have recently been identified in this zone (Han et al., 2010; Xu et al., 2013).

The Zongnaishan–Shalazhashan Zone (ZSZ) is bounded by the Enger Us Fault to the north and the Qagan Qulu Fault to the south and is covered by Cenozoic sediments to the west and sinistrally displaced by the NE–SW trending Zuunbayan Fault and Langshan Fault (Fig. 1b). Its eastern extension is unclear. Permian granitoids and gabbros and early Triassic granitoids make up the main body of the Zongnaishan and Shalazhashan (W. Zhang et al., 2013a; Shi et al., 2014a, b). Minor late Carboniferous granitoids also occur in this region (Yang et al., 2014). The Amushan Formation is the dominant Paleozoic sedimentary units in this area and is mainly composed of volcanic rocks, neritic carbonate rocks and clastic sediments, which has recently been explained to have been deposited during the Carboniferous to early Permian (Yin et al., 2016). Some Precambrian high-grade metamorphic rocks are exposed in the Zongnaishan area, which yielded zircon U–Pb ages of ca 1.4 Ga (Shi et al., 2016). However, the ca.1.4Ga magmatic events are rare in the Alxa Block and the NCC. Moreover, available geochronological data do not support the existence of Archean–Paleoproterozoic basement in the ZSZ. Some authors hence suggested that the ZSZ has an affinity with the microcontinental blocks in the CAOB (Zhang et al., 2015b; Shi et al., 2016).

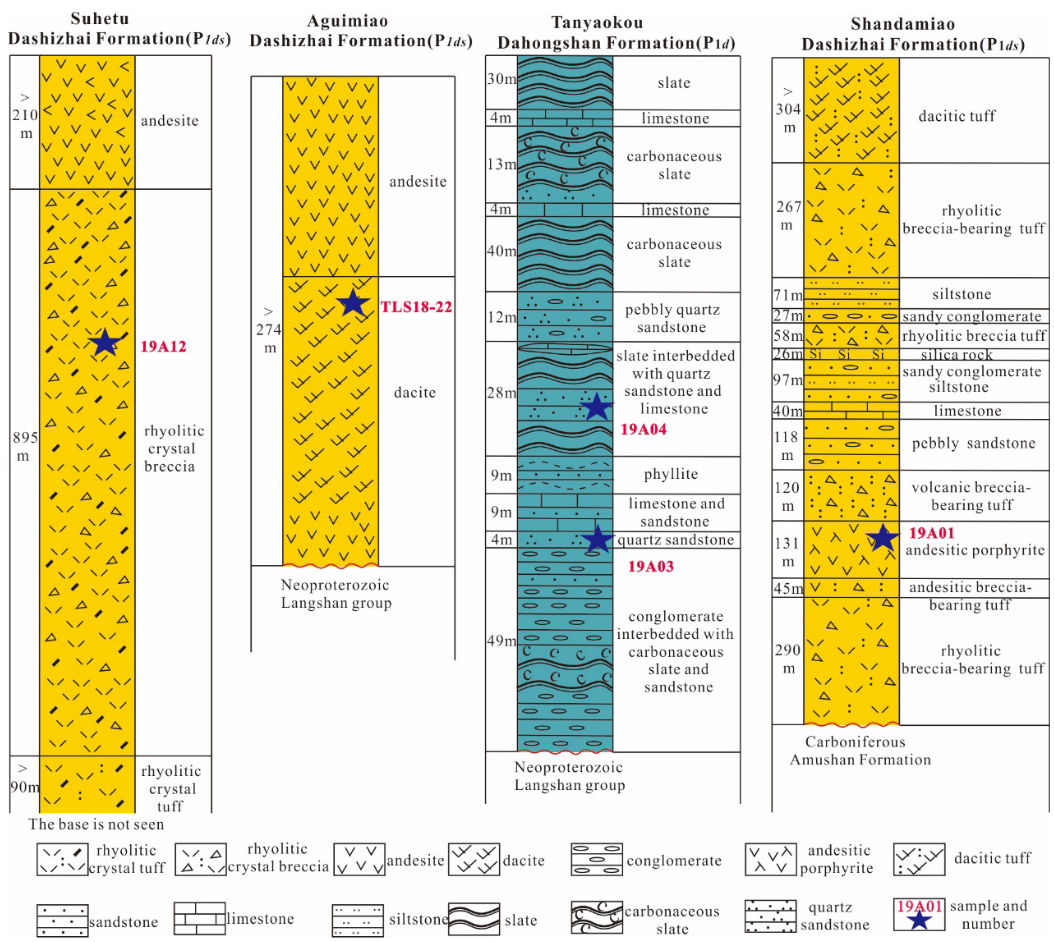

Figure 4. Stratigraphic column of Permian volcano–sedimentary rocks from the Langshan region. Modified from BGMRNM (1991). Positions of the samples in this study are indicated.

The Nuoergong – Langshan Zone (NLZ) is located to the south of the Quagan Qulu ophiolite belt (Fig. 1b). In this zone, Precambrian metamorphic basement rocks are widely exposed along the Bayanwulashan, Longshoushan, Beidashan, and Langshan (J.X. Zhang et al., 2013b; Gong et al., 2016; Dan et al., 2012). Neoproterozoic to early Paleozoic magmatic rocks are sporadical (Dan et al., 2014a; Liu et al., 2016b). Instead, large volumes of Carboniferous to Permian igneous rocks, including granites, diorites, mafic–ultramafic rocks and intermediate–acid volcanic rocks are exposed in this zone. In the Langshan region, Carboniferous to Permian granite suffered extensive ductile shear deformation. Besides, a Triassic alkaline–rich intrusion belt also occurs in the NLZ (Ren et al., 2005).

3. Geology of the Langshan zone

The Langshan zone, trending northeast for nearly 160 km along the western margin of the Hetao Garben, is part of the NLZ in the northeastern Alxa Block (Fig. 1b). Precambrian rocks in this belt include late Archean to Paleoproterozoic metamorphic rocks (the Wulashan Group and the Diebusige Group) and Neoproterozoic meta–sedimentary rocks (the Langshan Group) (Fig. 2). The Neoproterozoic Langshan Group dominantly consists of crystalline limestone, quartz sandstone, mica–quartz schist and carbonaceous schist, quartzite. Paleozoic sedimentary record is rare in this belt, and only Permian volcanic rocks and minor clastic sediments are sporadically exposed in the Shandamiao, Tanyaokou, Aguimiao and Suhetu areas (Fig. 2). In the Shandamiao area, the Permian strata are dominantly composed of rhyolitic tuff, andesitic porphyrite, dacitic tuff, and minor sandstone and siltstone. In the Aguimiao area, the volcanic rocks, mainly andesite and dacite in composition, are unconformably overlying the Langshan Group (Fig. 4). The rhyolite with rhyotaxitic structure (Fig. 7f) and andesite distribute in the Suhetu area, which was intruded by Triassic alkaline–rich rocks. The volcaniclastic rocks along the Langshan belt were not formally named by the previous 1:200,000 mapping. Recently, these rocks were mapped as the Dashizhai Formation and attributed to early and middle Permian (Guo et al., 2017). The Dahongshan Formation in the Tanyaokou area is mainly conglomerate, carbonaceous slate, quartz sandstone, and limestone, which unconformably overlies on the Neoproterozoic Langshan Group (Fig. 7a, b). This formation was considered to be formed in the early Permian based on stratigraphic correlation (BGMRNHAR, 1982) but chronological data are lacking. Despite its significance in evaluating the tectonic setting, the Permian strata in the Langshan belt have hitherto been poorly investigated.

In the late Paleozoic, the Langshan belt experienced extensive thermo–tectonic and deformation events in response to the southward subduction and closure of the Paleo–Asian Ocean plate along the northern margin of the Alxa Block. Large volume igneous, including granitoids, diorite, basalt, andesite and minor mafic to ultra–mafic rocks were emplaced during this period (Feng et al., 2013; Peng et al., 2013; Dan et al., 2014b; J.J Zhang et al., 2016b). A series of NE–SW thrust faults with SE or NW dips widely developed in the Langshan belt (Fig. 2). Widespread folds and thrusts deformation are also observed in this area. The crystalline limestone, sandstone, and quartzite in the Neoproterozoic Langshan group suffered intense compression to form overturned isoclinal folds (Fig.5b, c, d). Their hinge lines are subhorizontal to slightly dipping and strike to the northeast or southwest (Fig. 5b). The Paleoproterozoic Diebusige Group and the Neoproterozoic Langshan Group are intruded by felsic veins. These veins intruded roughly along the foliation and have also been folded (Fig. 5e, f), indicating these folds developed after the intrusion of felsic veins. In contrast, some felsic veins invaded the core of folds but were not folded (Fig. 5g), suggesting

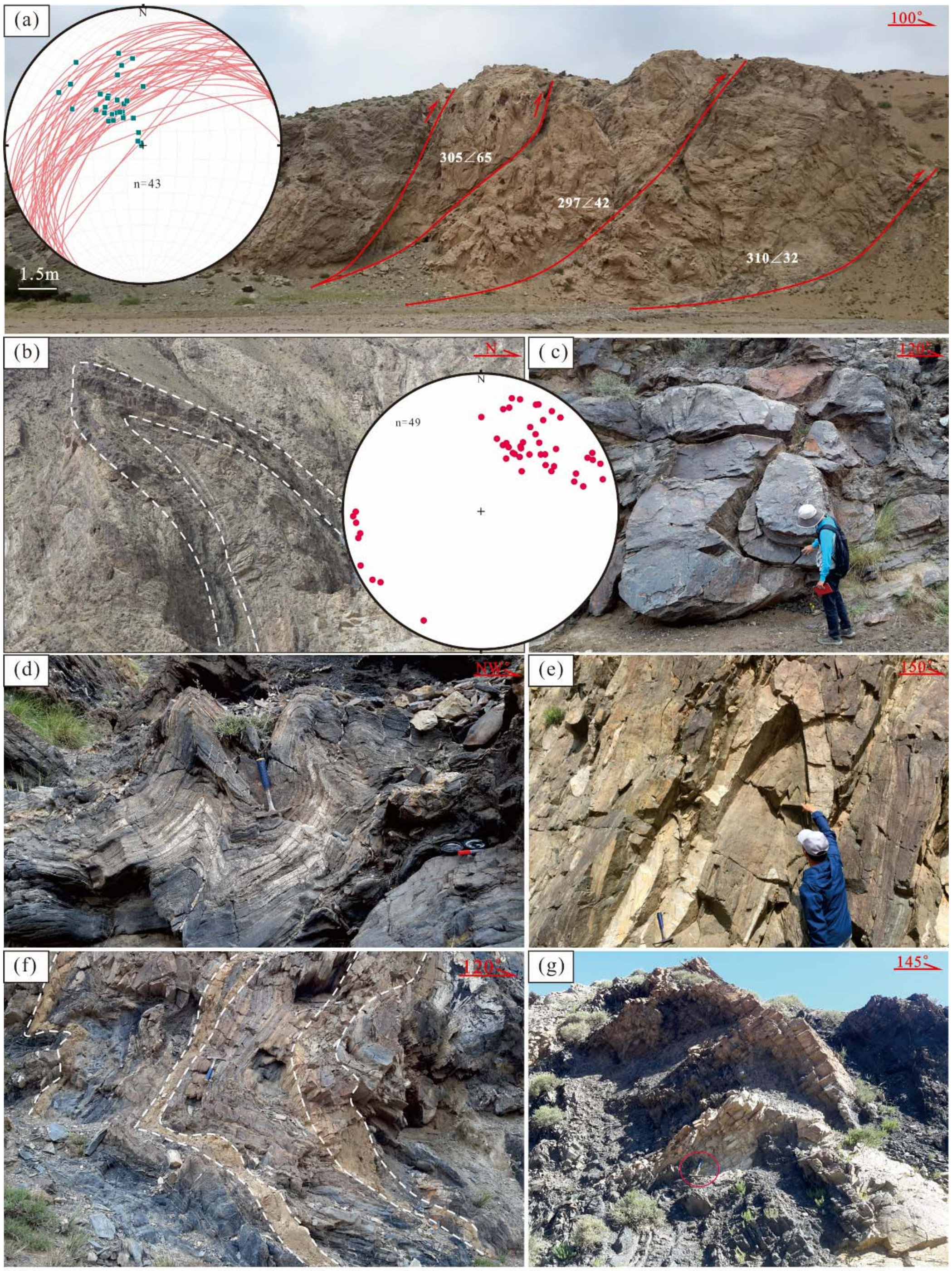

Figure 5. (a) Thrust faults in Permian granite. The great circles in the stereographic projection are fault planes, green spots are slickenlines of the fault planes. (b) Isoclinal overturned fold of crystalline limestone in the Langshan Group; the red spots in the stereographic projection indicate fold hinges. (c) folded thick-bedded quartzite in the Langshan Group. (d) M–type fold in the Langshan Group. (e) Felsic veins intruding the Diebusige Group were also folded (f) Felsic veins intruding the Langshan Group were also folded. (g) Felsic veins intrude the fold core.

intrusion after deformation. Large-scale thrusts and nappes were documented in

Permian granitic plutons (Fig. 5a). The fault planes strike NE–SW and dip to NW, pointing to a southeastward thrusting (Fig. 5a).

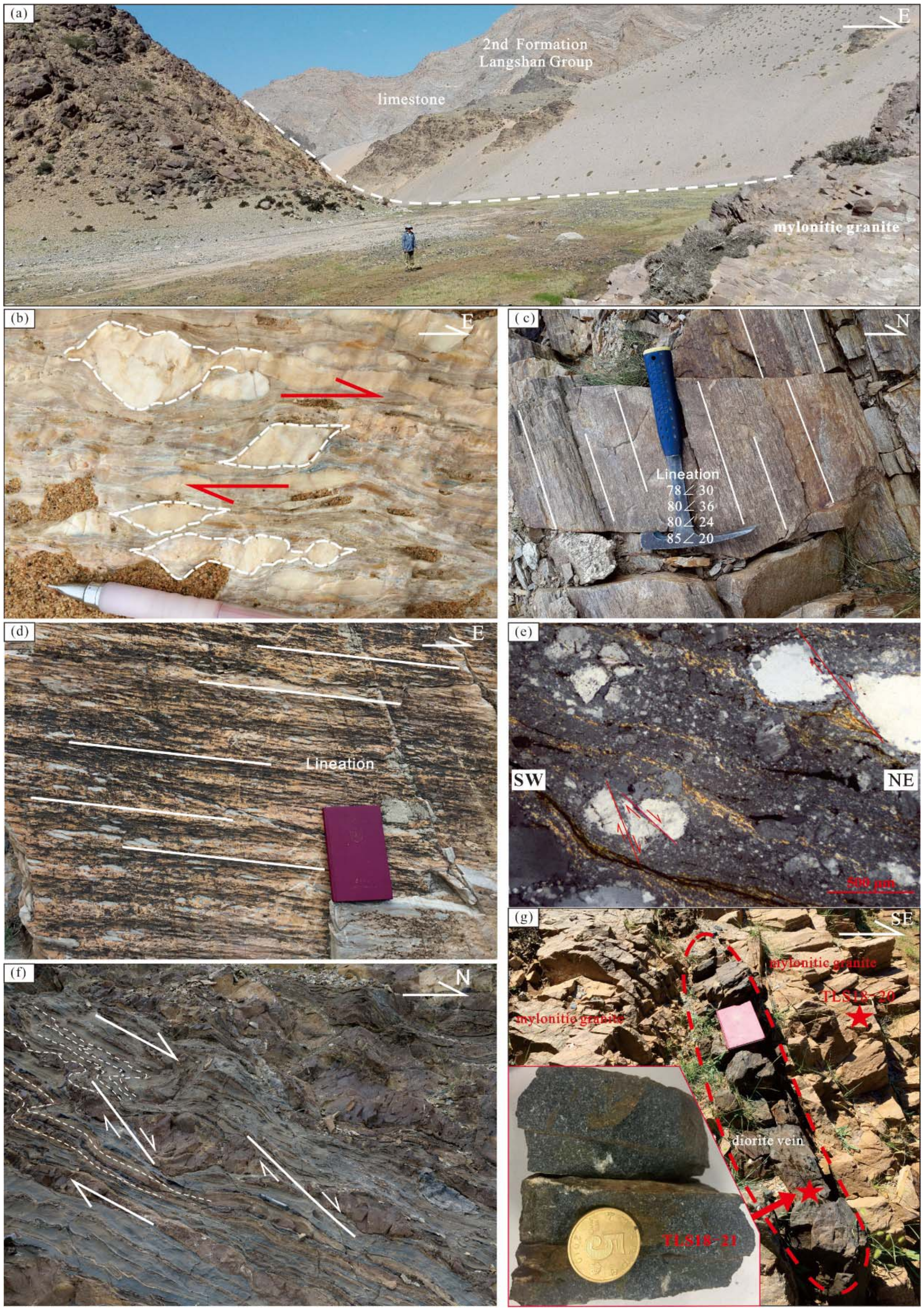

Figure 6. (a) Dextral ductile strike–slip shear between the Neoproterozoic Langshan Group and the Permian granite pluton. (b) σ–type asymmetric calcite porphyroclast in the Langshan Group, indicating dextral shearing. (c)

mylonitized granite. (d) mylonitized limestone in the Langshan Group. (e) Photomicrographs of granitic mylonite in cross–polarized light suggest dextral strike–slip shear sense. (f) Deformation of nodular chert and crystalline limestone in the Langshan Group, indicating dextral shearing. (g) An undeformed diorite vein intruded the granitic mylonite.

Strike–slip shear is also widely distributed in the Langshan belt. There are three mylonite belts in the southwestern Langshan belt (Fig. 3). The quartzite and muscovite quartz schist from the Neoproterozoic Langshan Group suffered extensive sinistral ductile shearing. Gong et al. (2017) obtained ~379 Ma and ~356 Ma $^{40}Ar/^{39}Ar$ ages from felsic mylonites, indicting deformation in the Late Devonian. Besides, the NE–trending sinistral ductile shearing along the Langshan – Bayanwula Shan in the southeastern part of the study area was interpreted as the result of the collisional between the Yangtze and North China Blocks during the Triassic (J. Zhang et al., 2013c).

In our field mapping, we discovered, for the first time, a ductile dextral shear zone, which developed along the boundary between the Neoproterozoic Langshan Group and the Permian granite pluton (Fig. 3 and Fig. 6a). The dextral shear zone extends continuously for ~30 km in our mapping area with a maximum width of ~1 km and is covered by Quaternary sediments further to the southwest (Fig. 3). The mylonitic foliations in the shear zone generally strike NEE–SWW and dip to the north or south at steep to nearly vertical angles (Fig. 3a and b). In the study area, the mylonitic foliations were partly dislocated by a series of nearly north–south left–lateral strike–slip faults (Fig. 3), which induced a clockwise rotation and thus formed nearly east–west foliations (Fig. 3a, b). The stretching lineations in the shear zone are defined by the preferred alignment of mica, feldspar, and quartz ribbon. Most stretching lineations are subhorizontal in the shear zone (Fig. 3a, b and Fig. 6c). Based on the field investigation and microscopic observation, kinematic fabrics are widely distributed in the granitic mylonite belt, including σ–type asymmetric quartz augens, fish–like structures and quartz recrystallized tails (Fig. 6e). Several types of microstructures can also be observed, such as undulatory extinction and deformation bands in deformed quartz grains, dynamic recrystallization, and core–mantle structures (Fig. 6e). The Neoproterozoic Langshan Group has also undergone extensive deformation near the boundary. Large volumes of crystalline limestone in this Group have been mylonitized (Fig. 6d). Several kinematic indicators developed, including boundinage of chert and σ–type asymmetric calcite porphyroclast (Fig. 6b, f). All these deformation characteristics indicate a dextral sense of shearing.

Figure 7. Field and photomicrographs of Permian clastic sediments and volcanic rocks. (a) and (b) The angular unconformity between the Permian Dahongshan Formation and the Neoproterozoic Langshan Group; (c) Conglomerate from the Permian Dahongshan Formation; (d) and (g) Field and photomicrographs of andesite from the Aguimiao area; (e) and (h) Field and photomicrographs of dacite from the Shandamiao area; (f) and (i) Field and photomicrographs of rhyolite from the Suhetu area.

4. Sample description

To evaluate the age and tectonic setting for magmatism, sedimentation and ductile deformation, different types of samples were collected and analyzed from the Langshan belt in this study. The sampling locations are shown in Fig. 2, 3 and 4. The GPS coordinates of the samples are presented in Appendix Table S1. Three volcanic samples (19A01, 19A12 and TLS18–22) were collected for zircon U - Pb dating, as well as major and trace element analyses. Sample 19A01 is a dacite collected from the Shandamiao area, which contains phenocrysts of euhedral–subhedral potassium feldspar (25–30 vol.%), plagioclase (10–15 vol.%) and xenomorphic quartz (10–15 vol.%). The groundmass shows cryptocrystalline texture that is mainly composed of plagioclase, quartz and accessory minerals, such as zircon and apatite. The sample (19A12) was collected from the Suhetu area and is rhyolite in composition, containing ~20 vol.% plagioclase phenocrysts and ~10 vol.% quartz phenocrysts. The hyalopilitic texture groundmass is composed of plagioclase microlites and volcanic glass. Sample TLS18–22 is light-green andesite collected from the Aguimiao area, which mainly consists of long prismatic plagioclase with slight alteration (60 vol.%) and hornblende and minor pyroxene. Two quartz sandstone samples (19A03 and 19A04) from the Dahongshan Formation in the Tanyaokou areas were also collected for detrital zircon U–Pb dating. Moreover, two granitic mylonites (TLS18–20 and TLS18–23) in the shear zone and an intruding undeformed diorite vein (TLS18–21) were also collected for zircon U – Pb dating (Fig. 6g).

5. Analytical results

Analytical methods are presented as supplementary material in Tables S1. Zircon U–Pb dating and whole–rock major and trace element compositions of volcanic rocks are available in supporting information Tables S1and S2, respectively. In this study, $^{207}Pb/^{206}Pb$ ages are adopted for zircons older than 1Ga, while $^{206}Pb/^{238}U$ ages are used for zircon younger than 1Ga.

5.1. Zircon U–Pb dating

Zircon grains from sample 19A01 (dacite) are mostly euhedral, with a length of 50~200um. They commonly show oscillatory zoning in CL images and have Th/U ratios between 0.19 and 0.90, indicating a magmatic origin. Zircon U–Pb dating yielded a weighted mean $^{206}Pb/^{238}U$ age of 263 ± 3 Ma (MSWD = 0.18, n = 5; Fig. 8a). This is consistent with the U–Pb ages recently reported from intermediate–basic volcanic rocks north to the sample site (Guo et al., 2017). Twenty-one analyses yielded older ages clustered at 442±2Ma (Fig. 8a), which are interpreted as captured zircon ages. This is consistent with the fact that the underlying rocks of Permian volcanic rocks are Silurian diorites (Wang et al., 2015).

Sample TLS18–22 (andesite) and 19A12 (rhyolite) were collected from the Aguimiao and Suhetu areas in the central and southwestern Langshan belt, respectively. Zircons from these two samples are euhedral and display clear oscillatory growth zoning in CL images. Twenty-seven zircon grains from the andesite (TLS18–22) are analyzed, yielding a weighted mean $^{206}Pb/^{238}U$ age of 270 ± 3 Ma

(MSWD=0.07; Fig. 8c), whereas 22 analyses for the rhyolite (19A12) give a weighted mean age of 273 ±2 Ma (MSWD=0.33; Fig. 8b). These ages are interpreted as the crystallization age of the andesite and rhyolite. Besides, zircon xenocrysts with concordant age of 2538 Ma and 987 Ma are also obtained from the rhyolite (TableS1).

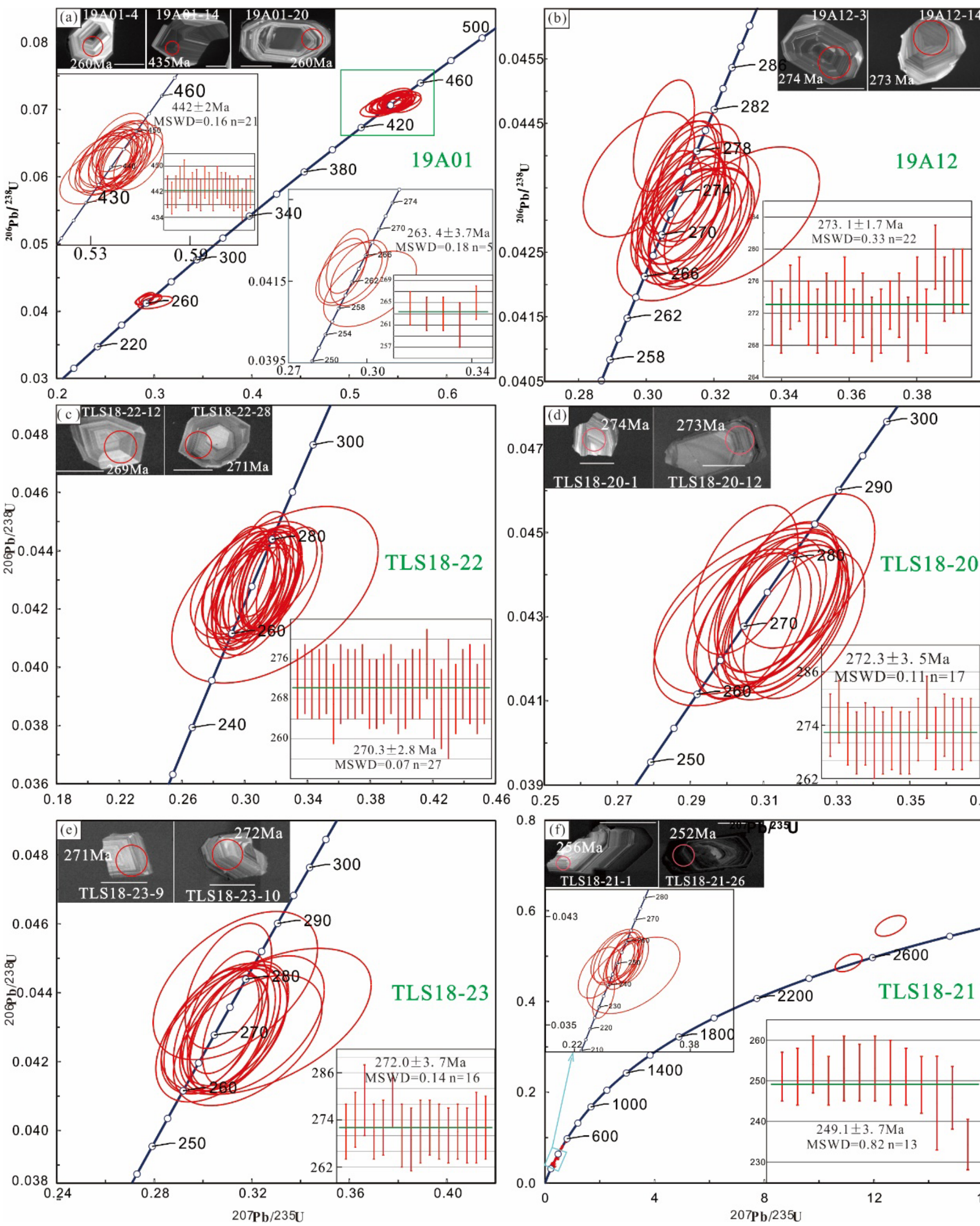

Figure 8. Zircon U–Pb concordia diagrams and histograms for the volcanic rocks and plutons in the Langshan area.

(a) Dacite; (b) rhyolite; (c) andesite; (d) and (e) mylonitized granites; (f) undeformed diorite vein

Two granitic mylonite samples (TLS18–20 and TLS18–23) from the dextral shear zone yielded identical zircon U–Pb ages of 272±3.5 Ma and 272±4 3.7 Ma (Fig. 8d, e). Thirteen out of 35 analyzed zircons from the intruding undeformed diorite vein (TLS18–21) form a tight cluster, with a weighted mean $^{206}Pb/^{238}U$ age of 249±4 Ma (MSWD=0.82), which is interpreted as the crystallization age of the undeformed diorite vein. Other analyses mainly yielded two groups of ages, with weighted $^{206}Pb/^{238}U$ ages of 281Ma (MSWD=1.4, n = 7) and 330Ma (MSWD=1.9, n = 6) respectively, which are interpreted as ages of xenocrysts; indeed, early Carboniferous (ca. 330Ma) and early Permian (ca. 280Ma) magmatic rocks have been widely documented in the eastern Alxa Block (Shi et al., 2012; J.J Zhang et al., 2016b; Dan et al., 2016; Zheng et al., 2019b). The remaining two analyses (spots 13 and 14) show much older ages around 2.5 Ga, which are considered as the captured zircons from the crystalline basement (Fig. 8f). These data thus contain the time of the dextral ductile shear deformation between 272 Ma and 249 Ma.

Two sandstone samples (19A03 and 19A04) from the Dahongshan Formation in the Tanyaokou area are used for detrital zircon U-Pb dating. Most zircon grains are euhedral to subrounded, and a few are rounded in shape. Most of the zircon grains exhibit oscillatory zoning with Th/U ratios of 0.11 – 2.79. The ages from sample 19A03 mainly range from 259 Ma to 2484 Ma and cluster around four prominent age peaks at ca. 261 Ma, 289 Ma, 305 Ma, and 1352 Ma, respectively (Fig. 9b). The ages from sample 19A04 mainly range from 272Ma to 3462 Ma, with two main age peaks (318 Ma and 1947 Ma, respectively) and several secondary age peaks (273 Ma, 2388

Ma, and 2509 Ma; Fig. 9d). The youngest detrital zircon age peaks from the two samples constrain the maximum depositional ages of the Dahongshan Formation at 273 and 261Ma, respectively.

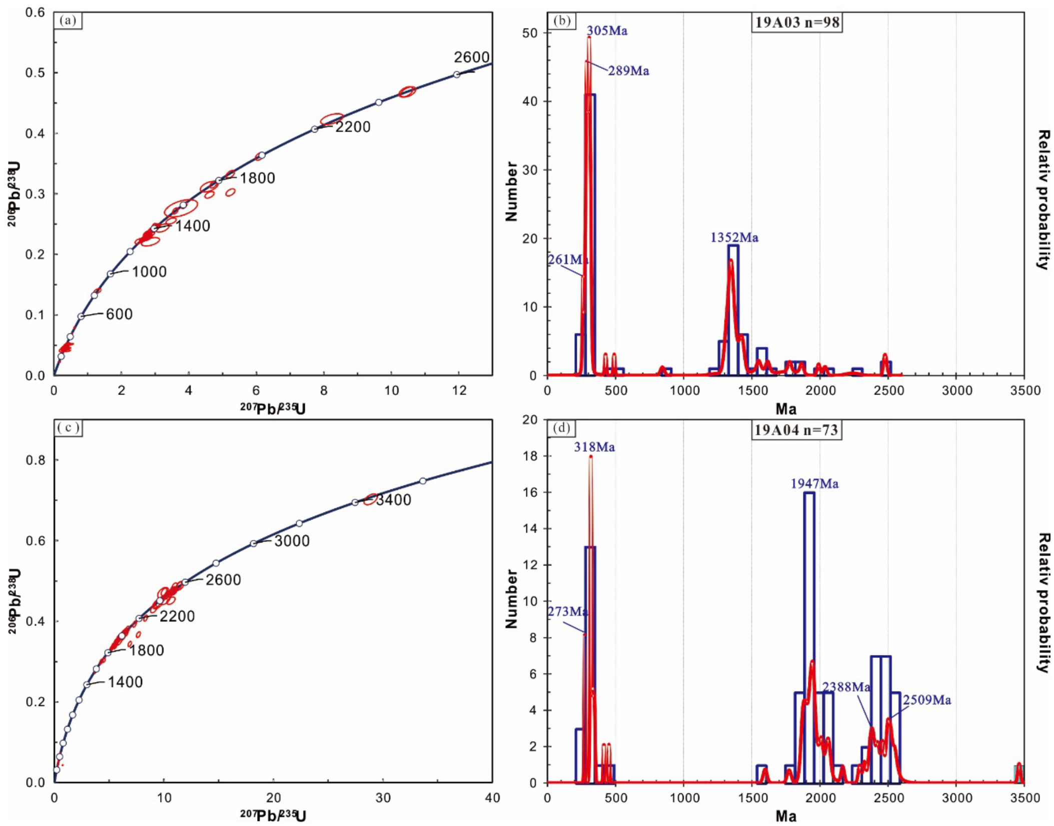

Figure 9. Concordia diagrams and age histograms of the detrital zircons from the Dahongshan Formation. Data with concordances between 90 and 110% are plotted.

5.2. Major and trace elements

Geochemical results for the Permian volcanic rocks in the Langshan belt are plotted in Fig. 10. Previous geochemical data of volcanic rocks from the Nuoergong – Langshan belt (Guo et al., 2017; Song et al., 2018b) are also plotted for comparison.

The Permian volcanic rocks in this study are intermediate to felsic with a wide range of SiO_2 contents (56.6–75.9 wt.%). The dacite and andesite show relatively high

LOI (loss on ignition, 2.2–5.0 wt. %), suggesting slight alteration or weathering. We thus use relatively immobile elements in the following discussion. In the Zr/TiO2 versus Nb/Y diagram, our samples are plotted in the andesite, dacite and rhyolite field (Fig. 10a), consistent with field and thin section observations (Fig. 7g, h and i). Chondrite–normalized REE patterns of these volcanic rocks are characterized by enrichments in the light rare earth elements (LREEs) relative to the heavy rare earth elements (HREEs), with La_n/Yb_n ratios of 9.78 – 14.12 and slightly negative Eu anomalies in the andesite and dacite (Eu/Eu* = 0.72 – 0.89) and significantly negative Eu anomalies (Eu/Eu* = 0.10 – 0.40) in the rhyolite (Fig. 10c; Table S2). The primitive–mantle normalized trace element diagram shows that these volcanic rocks are enriched in LILEs (e.g. K, Ba, Rb, and U) and depleted in HFSEs (e.g. Nb, Ta, P, and Ti) (Fig. 10d), typical for subduction–related magmas (Pearce and Peate. 1995).

6. Discussion

6.1. Sedimentary provenance and environment of the Permian strata

Before this study, no geochronology data have been reported for the Permian clastic sedimentary rocks in the Langshan region. Based on fossils and regional stratigraphic correlations, these clastic sediments were attributed to early Permian in age and named the Dahongshan Formation (BGMRNM. 1991). Detrital zircon U–Pb dating in this study suggests that the maximum depositional ages for samples 19A03 and 19A04 are 261Ma and 273Ma, respectively (Fig.9). A ca. 265Ma Zircon U-Pb age has been reported for volcanic rocks in the northern Langshan, which are probably correlative with the Dahongshan Formation (Guo et al., 2017). A significantly younger deposition age is unlikely considering the ubiquity of contemporary magmatic activity in this study area. Thus, the Dahongshan Formation is most likely deposited in the middle Permian (ca. 261 Ma).

The Dahongshan Formation shows a diverse lithology, including conglomerate, sandstone, slate, and minor limestone. Terrestrial plant fossils were also discovered in this formation (BGMRNM. 1991). The conglomerates contain pebbles with the diameter ranging from 2 mm to 50 cm and show poorly sorted characteristics (Fig. 7c), implying a short transportation distance and a proximal provenance from rapidly uplifting terranes. Detrital zircons from this formation are mainly composed of late Carboniferous to Permian and Palaeo–Mesoproterozoic grains (Fig. 9), suggesting denudation of relatively young magmatic rocks and ancient Precambrian basement. We compiled spectra in NLB. The age spectra of the Dahongshan Formation match well with the Paleozoic magmatic record and the Precambrian basement zircon ages (Fig. 11), consistent with a proximal source area for the Dahongshan Formation.

Different types of sedimentary basins may have distinct detrital zircon age distribution patterns. Generally, convergent settings are characterized by intense magmatic activities and therefore clastic sediments deposited in such tectonic settings contain a large proportion of zircon grains whose crystallization ages approximate the depositional age (Dickinson and Gehrels, 2009). In contrast, zircons from the underlying ancient basement are more common in collisional and extensional settings. Cawood et al. (2012) used detrital zircon age distribution patterns to identify tectonic settings. According to this approach (Figure as supplementary materials), together with the lithology and terrestrial plant fossils (BGMRNM. 1991), the Dahongshan Formation was most likely deposited in a retroarc foreland basin, where pyroclastic material with Carboniferous to Permian ages from the continental arc (see below) and sediments eroded from the Alxa Precambrian basements were deposited (Fig. 14c).

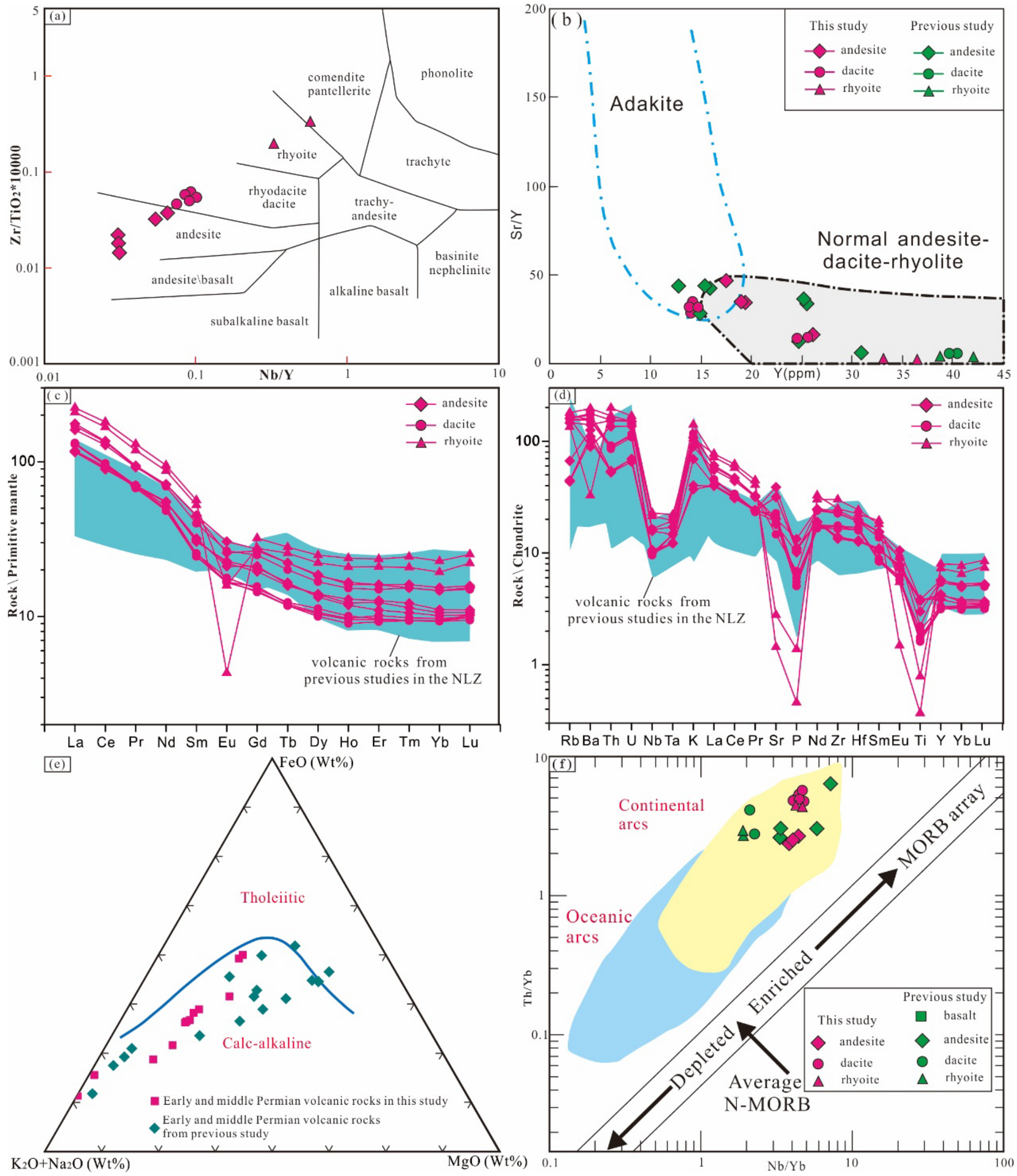

Figure 10. Geochemistry of the early and middle Permian volcanic rocks in the Nuoergong–Langshan zone. (a) Zr/TiO2 versus Nb/Y classification diagram after Winchester and Floyd, (1977); (b) Y versus Sr/Y diagram (after Defant and Drummond, 1993). (c) and (d) Chondrite - normalized rare earth element patterns and primitive mantle–normalized spider diagrams. Standardized values are from Sun and McDonough (1989). (e) AFM ternary diagram, after Irvine and Baragar, (1971). (f) Th/Yb–Nb/Yb diagram (after Pearce and Peate, 1995). Permian volcanic rocks from previous studies (Guo et al. 2017; Song et al. 2018b).

6.2 Tectonic setting of the Nuoergong–Langshan Zone during the Permian

The southernmost boundary of the CAOB in the Alxa Block has not been well constrained. Previous studies suggested that the ca. 300 Ma Enger Us ophiolite belt represents the suture zone between the CAOB and the Alxa Block (Wang et al., 1998; Zheng et al., 2014; Xie et al., 2014), whereas the ca. 275 Ma Qagan Qulu ophiolite belt was interpreted as the location of final closure of a back–arc basin (Zheng et al., 2014). The early Permian volcanic and plutonic rocks in the Nuoergong–Langshan belt (NLB) were therefore interpreted to have been generated in a post–collisional setting or a mantle plume related extensional setting (Zhang et al., 2012; Dan et al., 2014b, 2015). Evidence supporting this model mainly includes: (1) a short period for the magmatic flare-up, (2) crust–mantle interaction, and (3) magmatic mixing. We discount this model, however, based on the following geological observations: (1) the early Permian plutons have a much smaller scale and span a longer interval (290–270 Ma) compared to large igneous province (Bryan and Ernst, 2008); (2) the presence of the Permian Qagan Qulu ophiolite belt in the northern part of this belt did not support a post–collisional setting (Zheng et al., 2014); (3) volcanic and plutonic rocks from this belt display cal–alkaline composition and arc–like geochemistry (Guo et al., 2017; Song et al., 2018b); and (4) intensive Permian folding and thrusting indicate a compressional setting.

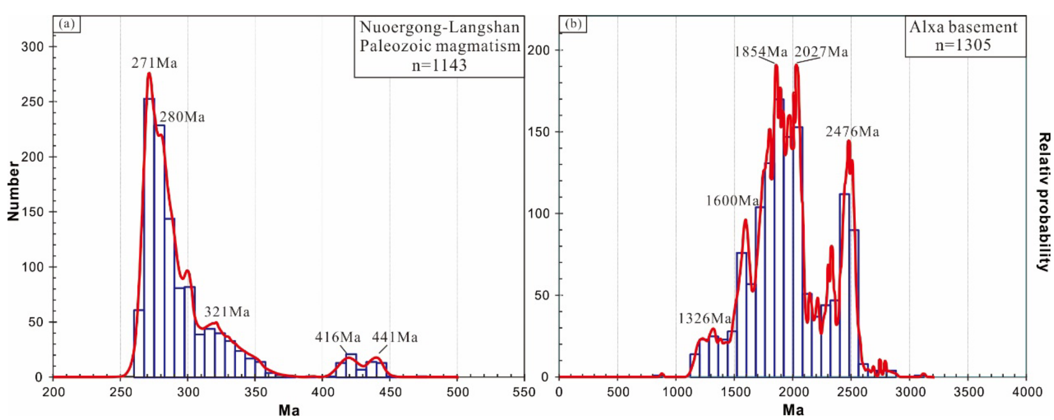

Figure 11. Compilation of zircon ages for (a) the Paleozoic magmatic rocks in the Nuoergong–Langshan zone and

(b) the Precambrian basement rocks of the Alxa Block. Data sources of the Paleozoic magmatic rocks in the Nuoergong–Langshan Zone are from (Liu et al. 2016b, 2017a, b; Dan et al. 2014b, 2016; Hu et al. 2015; Zhang et al. 2016b; Song et al. 2018b; Zheng et al. 2019a; Wang et al. 2015); data for the Alxa Precambrian basement rocks are from (Dan et al. 2012; Gong et al. 2012, 2016; Zhang et al. 2013b; Tian et al. 2019).

The early to middle Permian calc-alkaline volcanic rocks extend nearly 300 km along the Nuoergong-Langshan Belt (BGMRNM. 1991; Guo et al., 2017; Song et al., 2018b and this study). These volcanic rocks are characterized by relative enrichment of LILEs (e.g. K, Ba, Rb, and U) and LREE and depleted in HFSEs (e.g. Nb, Ta, P, and Ti) (Fig. 10d), indicating a subduction–related setting (Pearce and Peate. 1995). In the Th/Yb versus Nb/Yb discrimination diagram, all samples fall into the continental arc field (Fig. 10f), suggesting that the subduction of the PAO lasted at least to the early to middle Permian. The conclusion is also supported by geochemical data from Carboniferous to early Permian plutons in this belt (Shi et al., 2012; Peng et al., 2013; Liu et al., 2016a, 2017b; Song et al., 2018b; Zheng et al., 2019b). Song et al. (2018a) suggested that this belt probably extends eastward to the northern margin of the North China Craton, constituting an Andean–type magmatic arc along the northern margin of the Alax - NCC during the Carboniferous to middle Permian (Zhang et al., 2007a, 2009a, b; Liu et al., 2016a). The paucity of arc volcanic rocks probably results from intensive uplifting and denudation due to intraplate deformation, as documented in the Andean arcs (Ducea et al., 2015). In this context, the Permian mafic－ultramafic rocks (Feng et al., 2013), A–type and I–type granites (including high Sr/Y granodiorites) (Dan et al., 2014b), Adakitic rocks and Cu–Au mineralization (Li et al., 2010a, b) probably imply a slab window setting due to ridge subduction in the northern margin of the NLB.

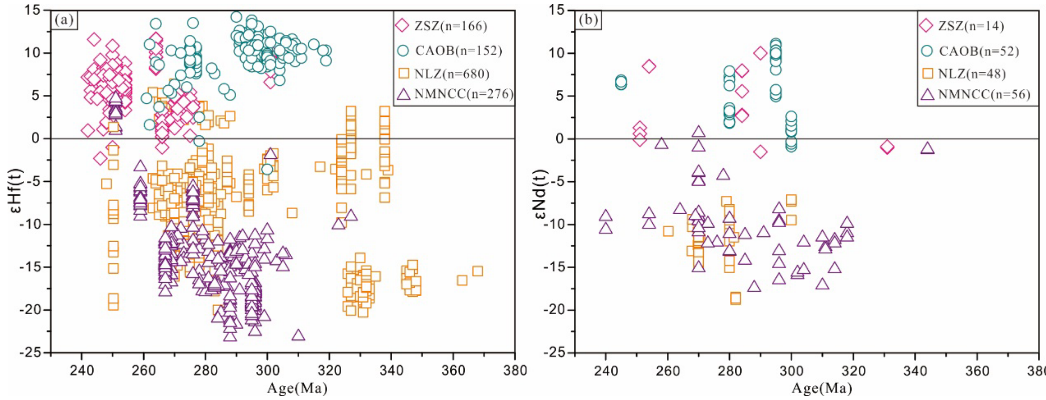

Figure 12. Compiled zircon Hf and whole–rock Nd isotopic compositions from Carboniferous to early Triassic plutons and volcanic rocks in the northern margin of the Alxa Block and adjacent regions. (a) Zircon Hf isotopic data are from (Shi et al. 2014a, b) for the Zongnaishan–Shalazhashan zone (ZSZ); (Zhang et al. 2018b, 2019; Shi et al. 2019; Wang et al. 2019) for the Central Asian Orogenic Belt (CAOB); (Pi et al. 2010; Peng et al. 2013; Hu et al. 2015; Liu et al. 2017a, b; Dan et al. 2014b, 2015; Liu et al. 2016a; Zheng et al. 2019a, b) for the Nuoergong–Langshan zone (NLZ); and (Ma et al. 2013; Zhang et al. 2007a, 2009a; Bai et al. 2013) for the North Margin of North China Craton (NMNCC). (b) Whole–rock Nd isotopic compositions in the ZSZ are from (Shi et al. 2018; Zhang et al. 2013a; Gan et al. 2018); the CAOB are from (Zhang et al. 2008, 2018b; Miao et al. 2008); the NLZ are from (Liu et al. 2017a; Dan et al. 2014b, 2015; Zheng et al. 2019a); and the NMNCC are from (Ma et al. 2013; Zhang et al. 2009a, b, 2016c; Ji et al. 2018).

It has been long proposed that the Zongnaishan–Shalazhashan zone (ZSZ) and Nuoergong–Langshan zone (NLZ) share similar basement and medium to high–grade metamorphism, and thus have a close tectonic affinity (e.g., Wang et al., 1994). However, the ca. 1.4 Ga Mesoproterozoic gneisses are the oldest documented basement rocks in the Zongnaishan area (Shi et al., 2016). In contrast, as part of the Alxa Block, the oldest basement rocks in the NLB are ca. 2.5 Ga TTG and Paleoproterozoic metamorphic complex (Dan et al., 2012; J.X. Zhang et al., 2013b; Gong et a., 2016), and ca. 1.4 Ga rocks are absent. More importantly, zircon Hf and whole–rock Nd isotopic compositions from the two belts differ significantly (Fig. 12). The ZSZ is characterized by juvenile isotopic compositions, comparable with those in the CAOB. Instead, the Carboniferous to early Triassic plutons and volcanic rocks from the NLZ have more negative zircon εHf and whole–rock εNd and are similar to those from the northern margin of the NCC. We argue that the ZSZ and NLZ have distinct Precambrian basement and Phanerozoic isotopic compositions and thus constitute two separate tectonic units. The ZSZ likely represents a microcontinent with the Mesoproterozoic basement in the CAOB. In fact, ca. 1.4 Ga magmatism has been widely documented in micro–continent blocks of the CAOB, including the central Tianshan Block (Hu et al., 2006; He et al., 2015a, 2018a), southern Beishan (Liu et al., 2011; He et al., 2015b; Yuan et al., 2019), southern Mongolia (Demoux et al., 2009) and the Xilinhot block (Han et al., 2017) but is rare in the Alxa Block and NCC. Therefore, the southern boundary between the CAOB and Alxa Block is probably the Qagan Qulu ophiolite, instead of the Enger Us ophiolite to the north.

6.3. Folding and thrusting and its tectonic implications

Accretionary orogens exhibit two distinct stress regimes and deformation behaviors as exemplified as those in the western and eastern Pacific, respectively. Cawood et al. (2009) grouped the accretionary orogens into the retreating and advancing types. The advancing orogeny induces intensive compression, folding and thrusting behind the arc (Stern. 2002; DeCelles. 2004; DeCelles et al., 2009; Ducea et al., 2015), resulting in crustal shortening and thickening and formation of retroarc foreland basins, as typified by the central Andes. In contrast, the retreating orogeny generally results in pervasive extension and back-arc rifting or seafloor spreading (Stern. 2002; Ducea et al., 2015).

During our field mapping, a large number of folds and thrusts were identified in the NLZ. The NE-SW trending overturned isoclinal folds in the Diebusige Group and the Langshan Group (Fig. 5b-f), as well as the large-scale southeastward thrusting faults in the Permian granitic plutons (Fig. 5a), indicate an NW–SE compressional deformation. Our previous study (Tian et al., 2017) indicated that these overturned isoclinal folds were probably related to the evolution of the PAO. Zircon U-Pb dating of folded felsic veins and unfolded intruding veins constrain the deformation age to middle to late Permian (J. Zhang, unpublished). Andesite and dacite from the Aguimiao area are characterized by high Sr (404-802 ppm), low Y (14.3-19.0 ppm) and Yb (1.58-1.88 ppm) contents, relatively high Sr/Y ratios (28-47) and slightly negative Eu anomaly and relatively low MgO contents (1.48-2.93 wt.%) (Table S2), which are similar to those of Adakitic rocks (Fig. 10b) derived from melting of the thickened mafic lower crust (Wang et al., 2006 and the references therein), supporting extensive crustal thickening during the late Carboniferous to middle Permian.

Such thrusting and folding and crustal thickening might have been related to oceanic ridge subduction (Feng et al., 2013), which has been widely recognized along the southern margin of CAOB (Tang et al., 2010, 2012a, b; Zhang et al., 2018a; see review in Windley et al. 2018).

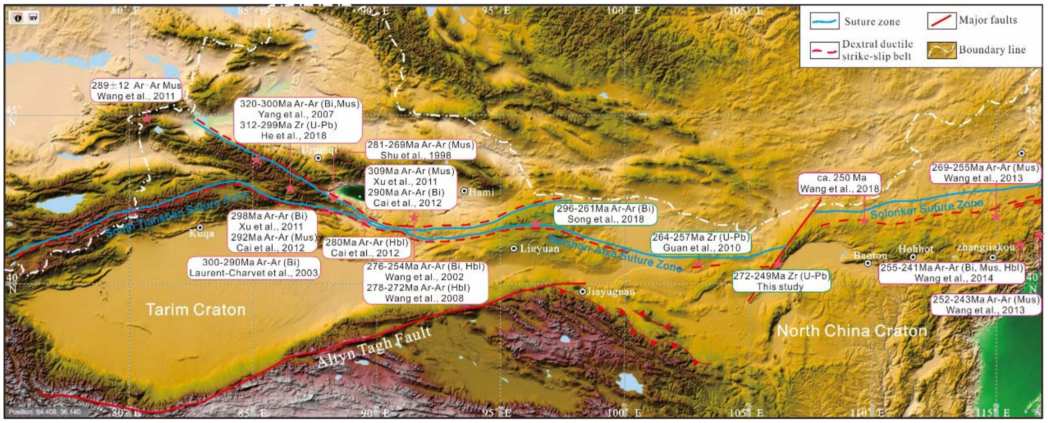

Figure 13. $^{40}Ar/^{39}Ar$ and zircon U–Pb dating constraint the dextral ductile strike–slip shearing in the south margin of CAOB, (background figure is downloaded from https://www.ngdc.noaa.gov/mgg/global/).

6.4. Timing of dextral strike–slip and its tectonic implications

The South Tianshan and Solonker suture zones are regarded as the locations of final subduction and closure of the PAO in the western and eastern parts of the southern CAOB, respectively. There is a consensus that the PAO closed in a scissor-like manner along the southernmost margin of the CAOB, with the closure time becoming younger from west to east, i.e. the late Carboniferous in the South Tianshan suture (Han et al., 2011; Klemd et al., 2015; Zhang et al., 2015a, 2016a; Wang et al., 2018a), the middle to late Permian in the Beishan and northern Alxa Block (Guo et al., 2012; Mao et al., 2012; Feng et al., 2013; Liu et al., 2017b, 2018a; Song et al., 2018a, b) and the Late Permian to Middle Triassic in the Solonker suture (Jian et al., 2010; Eizenhöfer et al., 2014; Eizenhöfer and Zhao et al., 2018).

Large–scale dextral strike–slip shear zone developed subparallel to the suture zone in the southern margin CAOB (Fig. 13). The deformation ages also become younger from the west to the east and are later than the final consumption of the PAO.

Based on field observations and isotopic dating over the last 20 years, the timing for the dextral strike–slip has been well constrained in the Tianshan belts (Fig. 13). In the western Tianshan, dextral ductile strike–slip may have initiated during 330–316 Ma (Wang et al., 2011). In the central Tianshan, dextral ductile shearing probably initiated at ca. 312–299 Ma (He et al., 2018b) and lasted to the early Permian (~270 Ma) (Shu et al., 1999; Laurent–Charvet et al., 2003; Yang et al., 2007; Xu et al., 2011a; Cai et al., 2012). Regional–scale dextral strike–slip zones in the eastern Tianshan formed during 290 – 272 Ma (Wang et al., 2008; Cai et al., 2012). Further west to the Kyrgyz western Tianshan, a late Carboniferous $^{40}Ar/^{39}Ar$ age of 312 Ma from a mylonite belt was regarded as the initiating age of dextral transpression and probably extended to the early Permian or middle Permian (Rolland et al., 2013).

In the middle section of southern CAOB, the Beishan orogenic belt underwent widespread ductile shearing deformation (Cai et al., 2012; Song et al., 2018c). Multiple ductile deformation events have been recorded by biotite $^{40}Ar–^{39}Ar$ ages of 323 ± 4 Ma, 296 ± 4 Ma, 261 ± 3 Ma in Beishan (Song et al., 2018c). Further east to the northern Alxa Block, Guan et al. (2010) constrained the deformation age between 264 Ma and 257 Ma based on zircon U – Pb dating of the mylonitic granite and the undeformed intruding diorite vein in the Tamusu area. In this study, our zircon U-Pb ages for the two granitic mylonites and the undeformed intruding diorite vein in the dextral shear zone constrain the deformation age between 272 Ma and 249 Ma.

In the eastern section of the southern margin of CAOB (i.e. northern margin of NCC), the dextral strike–slip has been constrained between 269 Ma and 241 Ma by

^{40}Ar–^{39}Ar dating from the Fengning – Longhua and the Kangbao – Weichang fault zone, in the Yinshan belt (Wang et al., 2013; Wang and Wan, 2014).

The large-scale strike-slip documented above may be akin to the present–day southern Qinghai–Tibet Plateau where large scale strike–slip occurred subparallel to the suture zone since the collision between the India block and Asia (Xu et al., 2011b). This large-scale dextral strike–slip throughout the southern CAOB probably resulted in eastward lateral extrusion of the thickened crust relative to the Tarim and North China Craton after the continental collision (Wang et al., 2008, 2009, 2011 and this study). Therefore, the final consumption of the PAO in the northern Alxa Block probably occurred before this process in the middle to late Permian.

6.5. Tectonic evolution of northern Alxa Block in late Paleozoic

Based on the above discussion, we propose an updated model for the final stage tectonic evolution of the PAO in the northern Alxa Block (Fig. 14).

During the early Carboniferous, the PAO subducted beneath the northern Alxa Block, forming an active continent arc (Liu et al., 2016a; Zheng et al., 2019b). Similar to microcontinents in the Central Tianshan and southern Beishan, the ZSZ is also considered to be a microcontinent within the PAO, which finally amalgamated with the northern ZHZ along the Enger Us suture zone at ca. 300 Ma (Zheng et al., 2014). Late Carboniferous adakites was recognized in the ZHZ, providing evidence for the subduction of the PAO (Shi et al., 2014a).

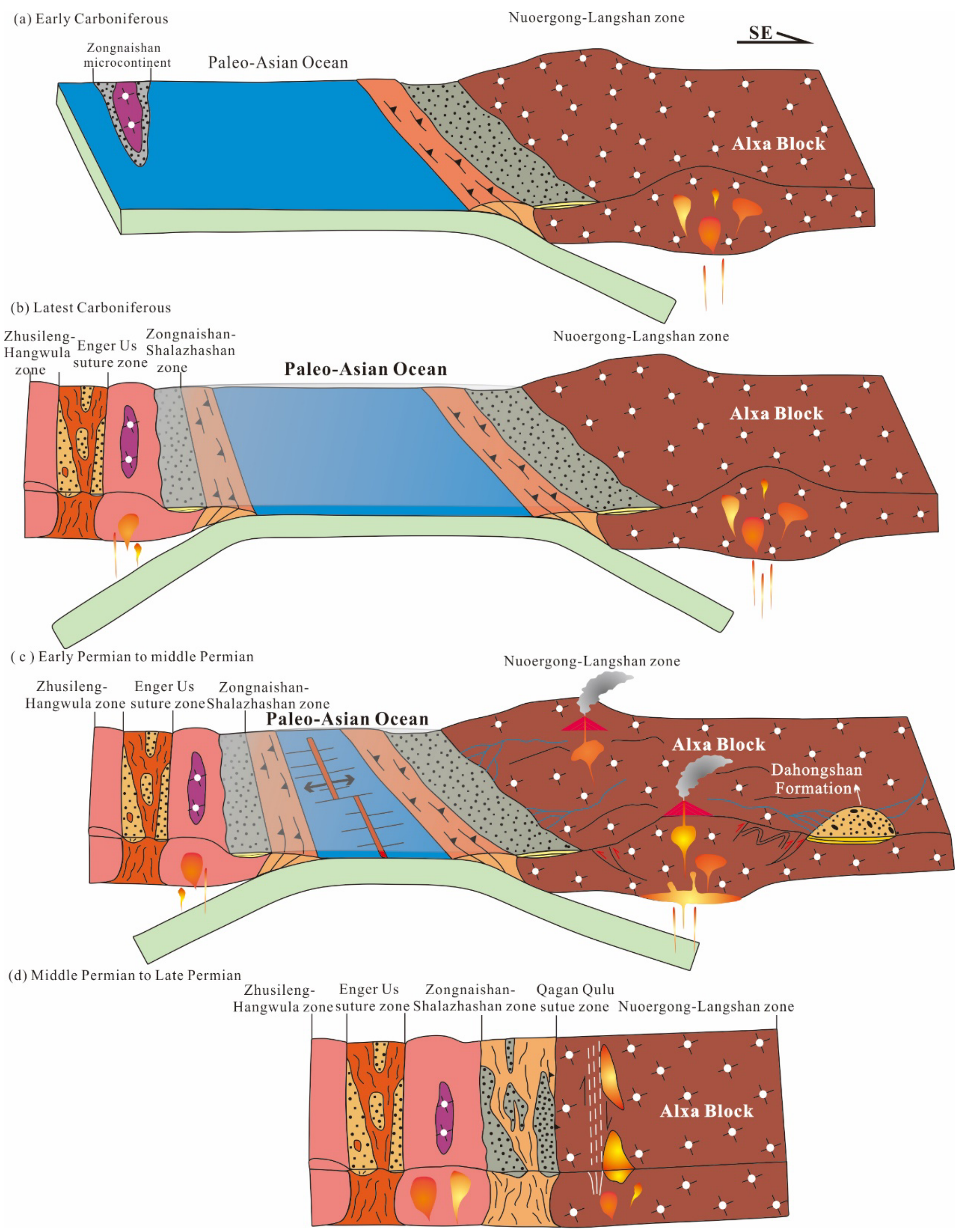

Figure 14. Schematic tectonic evolution for the northern Alxa Block relating to the final consumption of the Paleo-Asian Ocean (PAO). (a) The PAO subducted southeastward beneath the Alxa Block during the early Carboniferous; (b) the Zongnaishan–Shalazhashan microcontinent amalgamated with the Zhusileng–Hangwula arc along the Enger Us suture zone during the latest Carboniferous; (c) divergent double subduction of the PAO resulted in NW–SE compression during the early – middle Permian; (d) final closure of the PAO took place along the Qagan Qulu suture zone during the middle to late Permian, resulting in large-scale dextral strike–slip and eastward extrusion of the Central Asian Orogenic Belt.

In the early to middle Permian, the PAO started to diminish and close due to double–sided subduction. This led to widespread arc magmatism peaking at ca. 280–270 Ma in the NLZ and ZSZ (Yang et al., 2014; Dan et al., 2014b, 2015; J.J Zhang et al., 2016b; Zheng et al., 2019a and this study). Carboniferous to Permian arc-related volcanic rocks and sedimentary rocks (i.e. the Amushan Formation) are widespread along both sides of the Qagan Qulu suture zone (W. Zhang et al., 2013a; Zheng et al., 2017). During the middle to late Permian, an oceanic ridge within the PAO subducted beneath the Alxa Block (Feng et al., 2013), resulting in the collision between the ZSZ and the NLZ and forming the intervening Qagan Qulu suture zone. This also induced thrusting and folding and formation of a retroarc foreland basin, within which the Dahongshan Formation deposited. The Qagan Qulu suture zone in the Alxa Block probably marks the final closure of the PAO in the middle segment of the southern CAOB and is probably comparable with the Solonker suture zone to the east (Song et al., 2018a). After the collision, large-scale dextral ductile shear zones occurred, resulting in eastward lateral extrusion of the CAOB. We thus argue that the final consumption of the PAO occurred during the middle – later Permian in the northern Alxa Block.

7. Conclusions

(1) A ~300 km volcanic belt is identified in the Nuoergong – Langshan zone, which includes dacite, andesite, and rhyolite emplaced between 273 Ma and 263 Ma.

These rocks show cal–alkaline characteristics with enrichments of LILEs and depletion of HFSEs, indicating a continental arc environment.

(2) The PAO subducted southeastward along the northern Alxa Block in the early to middle Permian, resulting in NW-SE compression and large-scale folding and thrust faulting and crustal thickening in the Nuoergong-Langshan zone.

(3) The Dahongshan Formation mainly contains Carboniferous to Permian and Mesoproterozoic to Paleoproterozoic detrital zircons and probably had a proximal provenance from rapidly uplifting terranes, suggesting deposition in a back-arc foreland basin shortly after ~261 Ma.

(4) Large-scale dextral strike-slip occurred in the Langshan zone, which is constrained to take place between 272 Ma and 249 Ma using zircon U–Pb dating.

(5) Collectively, our data indicate that the final consumption of the PAO occurred in the middle – late Permian along the Qagan Qulu suture zone in the northern Alxa Block.

Acknowledgments

We have begun archiving our data in appropriate repositories, and the data archiving is underway. We plan to archive our Supplementary Material in the *4TU.Centre for Research Data*. Data and analytical methods for this article are either included as supporting information. We are grateful to Rongfeng Ge for his constructive comments and improvements on an early version of the manuscript. Special thanks are given to our team members (Qinglong Zhang, Junfeng Qu, Amirdin

Aierkin, Fahao Li and Pengfei Niu) for their assistance and patient guidance during field mapping. We also appreciate the assistance of Ziman Wu in an earlier version of the draft. This study was supported by the National Key R&D Plan of China (Grant Nos. 2017YFC0601402 and 2018YFC0603703).

References

Bai, X., Liu, S., Wang, W., Yang, P., Li, Q., 2013. U–Pb geochronology and Lu–Hf isotopes of zircons from newly identified Permian–Early Triassic plutons in western Liaoning province along the northern margin of the North China Craton: Constraints on petrogenesis and tectonic setting. International Journal of Earth Sciences 102, 671–685.

Bryan, S.E., Ernst, R.E., 2008. Revised definition of large igneous provinces (LIPs). Earth–Science Reviews 86, 175–202.

Bureau of Geology and Mineral Resources of Nei Mongol Autonomous Region, BGMRNM (1982). Investigation report of regional geology in Shandaoqiao region, China (in Chinese). P36–39 (In Chinese).

Bureau of Geology and Mineral Resources of Nei Mongol Autonomous Region, BGMRNM (1991). Regional geology of Nei Mongol Autonomous Region (in Chinese) (p. 725). Beijing: Geological Publishing House (In Chinese).

Cai, Z.H., Xu, Z.Q., He, B.Z., Wang, R.R., 2012. Age and tectonic evolution of ductile shear zone in the eastern Tianshan–Beishan orogenic belt. Acta Petrologica Sinica, 28(6): 1875–1895 (In Chinese with English abstract).

Cawood, P. A., Kröner, A., Collins, W. J., Kusky, T. M., Mooney, W. D., Windley, B. F., 2009. Accretionary orogens through Earth history. Geological Society, London, Special Publications, 318, 1 – 36.

Cawood, P.A., Hawkesworth, C.J., Dhuime, B., 2012. Detrital zircon record and tectonic setting. Geology 40:875 – 878

Demoux, A., Kröner, A., Liu, D., Badarch, G., 2009. Precambrian crystalline basement in southern Mongolia as revealed by SHRIMP zircon dating. Internal Journal of Earth Science 98, 1365–1380.

Dan, W., Li, X.H., Guo, J., Liu, Y., Wang, X.C., 2012. Paleoproterozoic evolution of the eastern Alxa Block, westernmost North China: evidence from in situ zircon U–Pb dating and Hf–O isotopes. Gondwana Research 21 (4), 838–864.

Dan, W., Li, X.–H., Wang, Q., Wang, X.–C., Liu, Y., 2014a. Neoproterozoic S–type granites in the Alxa Block, westernmost North China and tectonic implications: in situ zircon U–Pb–Hf–O isotopic and geochemical constraints. American Journal of Science 314 (1), 110–153.

Dan, W., Li, X. H., Wang, Q., Tang, G.J., Liu, Y., 2014b. An Early Permian (ca. 280 Ma) silicic igneous province in the Alxa Block, NW China: a magmatic flare–up triggered by a mantle–plume? Lithos 204, 144 – 158.

Dan, W., Wang, Q., Wang, X. C., Liu, Y., Wyman, D. A. & Liu, Y. S. (2015). Overlapping Sr–Nd–Hf–O isotopic compositions in Permian mafic enclaves and host granitoids in Alxa Block, NW China: Evidence for crust–mantle interaction and implications for the generation of silicic igneous provinces. Lithos 230, 133–145.

Dan, W., Li, X.H., Wang, Q., Wang, X.C., Wyman, D.A., Liu, Y., 2016. Phanerozoic amalgamation of the Alxa Block and NCC: evidence from Paleozoic granitoids, U–Pb geochronology and Sr–Nd–Pb–Hf–O isotope geochemistry. Gondwana Research http://dx.doi.org/10.1016/j.gr.2015.02.011.

Defant, M.J., Drummond, M.S., 1993. Mount St. Helens; potential example of the partial melting of the subducted lithosphere in a volcanic arc. Geology 21, 547 – 550.

DeCelles PG. 2004. Late Jurassic to Eocene evolution of the Cordilleran thrust belt and foreland basin system, western U.S.A. America Journal of Science 304:105–68

DeCelles, P. G., Ducea, M. N., Kapp, P., Zandt, G., 2009. Cyclicity in Cordilleran orogenic systems. Nature Geoscience 2, 251–257.

Dickinson, W.R., Gehrels, G.E., 2009. Use of U–Pb ages of detrital zircons to infer maximum depositional ages of strata: a test against a Colorado Plateau Mesozoic database. Earth and Planetary Science Letter 288:115–125

Ducea, M.N., Saleeby, J.B., and Bergantz, G., 2015. The Architecture, Chemistry, and Evolution of Continental Magmatic Arcs: Annual Review of Earth and Planetary Sciences 43, 299–331

Eizenhöfer, P.R., Zhao, G., Zhang, J., Sun, M., 2014. Final closure of the Paleo–Asian Ocean along the Solonker Suture Zone: constraints from geochronological and geochemical data of Permian volcanic and sedimentary rocks. Tectonics 33 (4), 441–463.

Eizenhöfer, P.R., Zhao, G., 2018. Solonker Suture in East Asia and its bearing on the final closure of the eastern segment of the Palaeo–Asian Ocean. Earth–Science Review 186, 153–172.

Feng, J. Y., Xiao, W. J., Windley, B. F., Han, C. M., Wan, B., Zhang, J. E., et al. (2013). Field geology, geochronology and geochemistry of mafic–ultramafic rocks from Alxa, China: Implications for Late Permian accretionary tectonics in the southern Altaids. Journal of Asian Earth Sciences, 78, 114–142. https://doi.org/10.1016/j.jseaes.2013.01.020.

Gan, L.S., Wu, T.R., Chen, Y., Zhang, W., Zhang, Z.Y., 2018. Geochronology and geochemical characteristics of the Shangdan pluton in the northern margin of the Alxa Block，Inner Mongolia and its tectonic implications. Acta Petrologica Sinica，34(11): 3359–3374 (In Chinese with English abstract).

Gong, J.H., Zhang, J.X., Yu, S.Y., Li, H.K., Hou, K.J., 2012. ~2.5 Ga TTG gneiss and its geological implications in the western Alxa Block, North China Craton. Chinese Science Bulletin 57, 4064–4076 (In Chinese with

English abstract).

Gong, J.H., Zhang, J.X., Wang, Z.Q., Yu, S.Y., Li, H.K., Li, Y.S., 2016. Origin of the Alxa Block, western China: New evidence from zircon U–Pb geochronology and Hf isotopes of the Longshoushan Complex. Gondwana Research 36, 359–375.

Gong, W.B., Hu, J.M., Wu, S.J., Liu, Y., Zhao, Y.F., 2017. Deformation characteristics, timing and significance of the Langshan sinistral strike–slip ductile shear zone, Inner Mongolia, Earth Science Frontiers, 24(3):263–275 (in Chinese with English abstract).

Guan, J., 2010. Study of the Aergashun ductile shear zone in Tamusu region of Alxa Youqi, Inner Mongolia. Master Dissertation of China University of Geoscience, P1–57 (in Chinese with English abstract).

Guo, Q. Q., Xiao, W. J., Windley, B. F., Mao, Q. G., Han, C. M., Qu, J. F., et al. (2012). Provenance and tectonic settings of Permian turbidites from the Beishan Mountains, NW China: Implications for the Late Paleozoic accretionary tectonics of the southern Altaids. Journal of Asian Earth Sciences, 49, 54 – 68. https://doi.org/10.1016/j.jseaes.2011.03.013.

Guo, S., Teng, X.J., Liu, Y., Teng, F., He, P., Wang, W.L., Tian, J., Duan, X.L., 2017. Geochemistry, chronology and Hf isotope features of the Permian intermediate–basic volcanic rocks in Wulanaobao area, Urad Houqi, Inner Mongolia and its geological significance. Journal of Geomechanics, 23:397–410 (in Chinese with English abstract).

Han, B. F., Zhang, C., Zhao, L., Ren, R., Xu, Z., Chen, J. F., Zhang, L., Zhou, Y. Z., Song, B., 2010. A preliminary study of granitoids in western Inner Mongolia. Acta Petrol. Mineral. 29:741–749 (in Chinese with English abstract).

Han, B.F., He, G.Q., Wang, X.C., Guo, Z.J., 2011. Late Carboniferous collision between the Tarim and Kazakhstan–Yili terranes in the western segment of the South Tian Shan Orogen, Central Asia, and implications for the Northern Xinjiang, western China. Earth Sci. Rev. 109, 74 – 93. http://dx.doi.org/10.1016/j.earscirev.2011.1009.1001.

Han, J., Zhou, J.B., Li, L., Song, M.C., 2017. Mesoproterozoic (~1.4 Ga) A–type gneissic granites in the Xilinhot terrane, NE China: first evidence for the break–up of Columbia in the eastern CAOB. Precambrian Research 296, 20 – 38.

He, Z.Y., Klemd, R., Zhang, Z.M., Zong, K.Q., Sun, L.X., Tian, Z.L., Huang, B.T., 2015a. Mesoproterozoic continental arc magmatism and crustal growth in the eastern Central Tianshan Arc Terrane of the southern Central Asian Orogenic Belt: geochronological and geochemical evidence. Lithos 236 – 237, 74 – 89.

He, Z.Y., Sun, L.X., Mao, L.J., Zong, K.Q., Zhang, Z.M., 2015b. Zircon U–Pb and Hf isotopic study of the gneiss and granodiorite from the southern Beishan orogenic collage: Mesoproterozoic magmatism and crustal growth. Chin. Sci. Bull. 60, 389 – 399 (in Chinese with English abstract).

He, Z.Y., Klemd, R., Yan, L.L., Lu, T.Y., Zhang, Z.M., 2018a. Mesoproterozoic juvenile crust in micro–continents of the Central Asian Orogenic Belt: evidence from oxygen and hafnium isotopes in zircon. Science Reports. 8, 5054.

He, Z.Y., Wang, B., Zhong, L.L., Zhu, X.Y., 2018b. Crustal evolution of the Central Tianshan Block: Insights from zircon U–Pb isotopic and structural data from meta–sedimentary and meta–igneous rocks along the Wulasitai – Wulanmoren shear zone. Precambrian Research 314, 111–128.

Hu, A.Q., Wei, J.G., Deng, W.F., Zhang, J.B., Chen, L.L., 2006. 1.4 Ga SHRIMP U–Pb age for zircons of granodiorite and its geological significance from the eastern segment of the Tianshan Mountains, Xinjiang, China. Geochemistry 35, 333 – 345 (in Chinese with English abstract).

Hu, J.M., Gong, W.B., Wu, S.J., Liu, Y., Liu, S.C., 2014. LA–ICP–MS zircon U–Pb dating of the Langshan Group in the northeast margin of the Alxa Block, with tectonic implications. Precambrian Research 255 (Part 2, no.

0), 756–770.

Hu, C.S., Li, W.B., Xu, C., Zhong, R.C., Zhu, F., Qiao, X.Y., 2015. Geochemistry and petrogenesis of Permian granitoids in the northwestern margin of the North China Craton: insights from the Dongshengmiao pluton, Inner Mongolia, International Geology Review, 57:14, 1843–1860, DOI: 10.1080/00206814.2015.1039087

Irvine, T.N., Baragar, W.R.A., 1971. A guide to the chemical classification of the common volcanic rocks. Can. J. Earth Sci. 8, 523 – 548. https://doi.org/10.1139/e71–055.

Ji, Z.J., Zhang, Z.C., Chen, Y., Li, K., Yang, J.F., Qian, X.Y., 2018. Geochemistry, geochronology, and Sr–Nd isotopic compositions of Permian volcanic rocks in the northern margin of the North China Block: implications for the tectonic setting of the southeastern Central Asian Orogenic Belt: International Journal of Earth Sciences, 107, 2143–2161.

Jian, P., Liu, D., Kröner, A., Windley, B.F., Shi, Y., Zhang, W., Tomurhuu, D., 2010. Evolution of a Permian intraoceanic arc – trench system in the Solonker suture zone, Central Asian Orogenic Belt, China and Mongolia. Lithos 118 (1), 169 – 190.

Klemd, R., Gao, J., Li, J.L., and Meyer, M., 2015, Metamorphic evolution of (ultra)–high–pressure subduction–related transient crust in the South Tianshan orogen (Central Asian orogenic belt): Geodynamic implications: Gondwana Research, v. 28, p. 1–25, https://doi .org/10.1016/j.gr.2014.11.008.

Laurent–Charvet, S., Charvet, J., Monié, P., Shu, L.S., 2003. Late Paleozoic strike–slip shear zones in eastern central Asia (NW China): new structural and geochronological data. Tectonics 22, 1009. doi: 10.1029/2001TC901047.

Le Maitre, R., Bateman, P., Dudek, A., Keller, J., Lameyre, J., Le Bas, M., Sabine, P., Schmid, R., Sorensen, H., Streckeisen, A., 1989. A classification of igneous rocks and glossary of terms. Recommendations of the IUGS Subcommission on the Systematics of Igneous rocks. Blackwell Scientific Publications, London.

Li, J. J., Zhai, Y. S., Sang, H. Q., Li, H. M., Zhang, Y. S., Liu, S. Y., Wang, S. G., Sun, Z. P., Liu, X. Y., 2010a. Metallogenic Epoch of the Oubulage Copper–Gold Deposit in the Alashan Area, Inner Mongolia Autonomous Region. Bulletin of Mineralogy, Petrology and Geochemistry 29 (4):323–327 (in Chinese with English abstract).

Li, J. J., Zhai, Y. S., Yang, Y. Q., Wang, Y. B., Li, C. D., Cui, L. W., Zhou, H. Y., Liu, X. Y., Liu, X. X., Li. S., 2010b. Re–discussion on the metallogenic age of Zhulazaga gold deposit in Alashan area, Inner, Mongolia: Evidence from zircon U–Pb SHRIMP age. Earth Science Frontiers 17 (2) 178–184 (in Chinese with English abstract).

Li, J.Y., Zhang, J., Qu, J.F., 2012. Amalgamation of North Craton with Alxa Block in the late of Early Paleozoic: evidences from sedimentary sequences in the Niushou Mountain, Ningxia Hui Autonomous Region, NW China. Geological Review 58, 208 – 214 (in Chinese with English abstract).

Liu, M., Zhang, D., Xiong, G., Zhao, H., Di, Y., Wang, Z., Zhou, Z., 2016a. Zircon U–Pb age, Hf isotope and geochemistry of Carboniferous intrusions from the Langshan area, Inner Mongolia: Petrogenesis and tectonic implications. Journal of Asian Earth Sciences 120, 139–158.

Liu, Q., Zhao, G. C., Sun, M., Han, Y. G., Eizenhöfer, P. R., Hou, W. Z., Zhang, X. R., Zhu, Y.L., Wang, B., Liu, D.X., Xu, B., 2016b. Early Paleozoic subduction processes of the Paleo–Asian Ocean: insights from geochronology and geochemistry of Paleozoic plutons in the Alxa Terrane. Lithos 262:546–560.

Liu, Q., Zhao, G.C., Han, Y.G., Eizenhöfer, P.R., Zhu, Y.L., Hou, W.Z., and Zhang, X.R., 2017a, Timing of the final closure of the Paleo–Asian Ocean in the Alxa terrane: Constraints from geochronology and geochemistry of late Carboniferous to Permian gabbros and diorites: Lithos, 274–275: 19–30, https://doi.org/10.1016/j. lithos.2016.12.029.

Liu, Q., Zhao, G., Han, Y., Eizenhöfer, P.R., Zhu, Y., Hou, W., Zhang, X., and Wang, B., 2017b. Geochronology and geochemistry of Permian to Early Triassic granitoids in the Alxa Terrane: Constraints on the final closure of the Paleo–Asian Ocean: Lithosphere, 9(4):665–680.

Liu, Q., Zhao, G.C., Han, Y.G., Zhu, Y.L., Wang, B., Eizenhöfer, P.R., Zhang, X.R., Tsui, R.W.S., 2018a. Timing of the final closure of the middle segment of the Paleo–Asian Ocean: Insights from geochronology and geochemistry of Carboniferous –Triassic volcano–sedimentary successions in western Inner Mongolia, China. GSA Bulletin 131 (5–6): 941–965. https://doi.org/10.1130/B32023.1

Liu, Q., Zhao, G., Han, Y., Li, X., Zhu, Y., Eizenhöfer, P.R., Zhang, X., Wang, B., Tsui, R.W., 2018b. Geochronology and Geochemistry of Paleozoic to Mesozoic Granitoids in Western Inner Mongolia, China: Implications for the Tectonic Evolution of the Southern Central Asian Orogenic Belt. The Journal of Geology126, 451–471.

Ma, X., Chen, B., Chen, J. F., Niu, X.L., 2013. Zircon SHRIMP U–Pb age, geochemical, Sr–Nd isotopic, and in–situ Hf isotopic data of the Late Carboniferous–Early Permian plutons in the northern margin of the North China Craton. Science China: Earth Sciences, 56: 126–144, doi: 10.1007/s11430–012–4456–6

Mao, Q.G., Xiao, W.J., Fang, T.H., Wang, J.B., Han, C.M., Sun, M., Yuan, C., 2012. Late Ordovician to early Devonian adakites and Nb–enriched basalts in the Liuyuan area, Beishan, NW China: implications for early Paleozoic slab–melting and crustal growth in the southern Altaids. Gondwana Research 22, 534 – 553

Pearce JA, Peate DW. 1995. Tectonic implications of the composition of volcanic arc magmas. Annual Review of Earth Planetary Science. 23:251 – 86

Peng, R.M., Zhai, Y.S., Li, C.S., Ripley, E.M., 2013. The Erbutu Ni–Cu deposit in the Central Asian Orogenic Belt: a Permian magmatic sulfide deposit related to boninitic magmatism in an arc setting. Economic Geology 108, 1879 – 1888.

Pi, Q.H., Liu, C.Z., Chen, Y.L., Li, Y.Q., Li, D.P., 2010. Formation epoch and genesis of intrusive rocks in

Huogeqi ore field of Inner Mongolia and their relationship with copper mineralization. Mineral Deposits 29, 437 – 451 (in Chinese with English abstract).

Ren, K.X., Yan, G.H., Mu, B.L., Cai, J.H., Tong, Y., Li, F.T., Zhao, F.S., Gu, L.B., Yang, B., Chu, Z.Y., 2005 Geochemistry and Nd, Sr , Pb isotopic characteristics of the alkali–rich intrusive rocks in Alxa Fault Block, Western Inner Mongolia and their implications. Earth Science Frontiers, 2005, 12(2):292–301 (in Chinese with English abstract).

Rolland, Y., Alexeiev, D.V., Kröner, A., Corsini, M., Loury, C., Monié, P., 2013. Late Palaeozoic to Mesozoic kinematic history of the Talas–Ferghana strike–slip fault (Kyrgyz West Tianshan) as revealed by 40Ar/39Ar dating of syn–kinematic white mica. Journal of Asian Earth Science 67–68, 76–92.

Şengör A.M.C, Natal'in BA, Burtman VS. 1993. Evolution of the Altaid tectonic collage and Palaeozoic crustal growth in Eurasia. *Nature* 364:299–307

Şengör, A.M.C., Natal' In, B.A., Sunal, G., van der Voo, R., 2018. The Tectonics of the Altaids: Crustal Growth during the Construction of the Continental Lithosphere of Central Asia Between ~750 and ~130 Ma Ago. Annual Review of Earth and Planetary Sciences 46, 439–494.

Shi, X. J., Tong, Y., Wang, T., Zhang, J. J., Zhang, Z. C., Zhang, L., Guo, L., Zeng, T. Geng, J. Z. (2012). LA–ICP–MS zircon U–Pb age and geochemistry of the Early Permian Halinudeng granite in northern Alxa area, western Inner Mongolia. Geological Bulletin of China 31, 662–670 (in Chinese with English abstract).

Shi, X.J., Wang, T., Zhang, L., Castro, A., Xiao, X.C., Tong, Y., Zhang, J.J., Guo, L., Yang, Q.D., 2014a. Timing, petrogenesis and tectonic setting of the Late Paleozoic gabbro–granodiorite–granite intrusions in the Shalazhashan of northern Alxa: constraints on the southernmost boundary of the Central Asian Orogenic Belt. Lithos 208–209,158–177.

Shi, X. J., Zhang, L., Wang, T., Xiao, X. C., Tong, Y., Zhang, J. J., Geng, J. Z., Ye, K., 2014b. Geochronology and geochemistry of the intermediate–acid intrusive rocks from Zongnaishan area in northern Alxa, Inner Mongolia, and their tectonic implications. Acta Petrol. Mineral. 33:989–1007 (in Chinese with English abstract).

Shi, X.J., Zhang, L., Wang, T., Zhang, J.J., Liu, M.H., Zhou, H.S., Yan, Y.T., 2016. Zircon geochronology and Hf isotopic compositions for the Mesoproterozoic gneisses in Zongnaishan area, northern Alxa and its tectonic affinity. Acta Petrol Sin. 32, 3518–3536 (in Chinese with English abstract).

Shi, G. Z., Wang, H., Liu, E. T., Huang, C. Y., Zhao, J. X., Song, G. Z., Liang, C., 2018. Sr–Nd–Pb isotope systematics of the Permian volcanic rocks in the northern margin of the Alxa Block (the Shalazhashan Belt) and comparisons with the nearby regions: Implications for a Permian rift setting? Journal of Geodynamics 115, 43–56.

Shi, Y., Yao, Y., Liu, Z.H., Liu, J., Wei, M.H., Gu, Y.C., Yang, F., Zhang, L., and Shi, S.S., 2019. Petrogeochemical characteristics, zircon SHRIMP U–Pb ages and Lu–Hf isotopic compositions of Late Carboniferous A–type granitoids, Yili area, Inner Mongolia (China). Geological Journal, 54(2): 770–790.

Shu, L.S., Charvet, J., Guo, L.Z., Lu, H.F., Laurent–Charvet, S., 1999. A large–scale Paleozoic dextral ductile strike–slip zone: the Aqqikkudug–Weiya zone along the northern margin of the Central Tianshan belt, Xinjiang, NW China. Acta Geologica Sinica 73 (2), 148–162 (In Chinese with English abstract).

Song, D., Xiao, W., Collins, A.S., Glorie, S., Han, C., Li, Y., 2018a. Final Subduction Processes of the Paleo–Asian Ocean in the Alxa Tectonic Belt (NW China): Constraints from Field and Chronological Data of Permian Arc–Related Volcano–Sedimentary Rocks. Tectonic 37, 1658–1687.

Song, D., Xiao, W., Collins, A., Glorie, S., Han, C., 2018b. Late Carboniferous–early Permian arc magmatism in the south–western Alxa Tectonic Belt (NW China): Constraints on the late Palaeozoic subduction history of the Palaeo–Asian Ocean. Geological Journal. 2018, 1–18.

Song, D.F., Xiao, W.J., Han, C.M., Tian, Z.H., Li, Y.C., 2018c. Accretionary processes of the central segment of Beishan: Constraints from structural deformation and 40Ar–39Ar geochronology. Acta Petrologica Sinica，34(7) : 2087–2098 (In Chinese with English abstract).

Stern, R. J., 2002. Subduction zones. Reviews of Geophysics, 40(4), 1012, doi: 10.1029/2001RG000108, 2002.

Sun, S.S., McDonough, W.F., 1989. Chemical and isotopic systematic of oceanic basalts: implications for mantle composition and processes. In: In: Saunders, A.D., Norry, M.J. (Eds.), Magmatism in the Oceanic Basins, vol. 42. Geological Society of London, pp.313 – 345.

Tang, G.J., Wang, Q., Wyman, D.A., Li, Z.X., Zhao, Z.H., Jia, X.H., Jiang, Z.Q., 2010. Ridge subduction and crustal growth in the Central Asian Orogenic Belt: evidence from Late Carboniferous adakites and high–Mg diorites in the western Junggar region, northern Xinjiang (west China). Chemical Geology 277, 281–300.

Tang, G.J., Wang, Q., Wyman, D.A., Li, Z.X., Zhao, Z.H., Yang, Y.H., 2012a. Late Carboniferous high εNd(t) – εHf(t) granitoids, enclaves and dikes in western Junggar, NW China: ridge–subduction–related magmatism and crustal growth. Lithos 140, 86 – 102.

Tang, G.J., Wyman, D.A., Wang, Q., Li, J., Li, Z.X., Zhao, Z.H., Sun, W.D., 2012b. Asthenosphere–lithosphere interaction triggered by a slab window during ridge subduction: trace element and Sr–Nd–Hf–Os isotopic evidence from Late Carboniferous tholeiites in the western Junggar area, NW China. Earth and Planetary Science Letter 329, 84–96.

Tian, R.S., Xie, G.A., Zhang, J., Qu, J.F., Aierkin, A., Li, F.H., Zhang, B.H., Zhao, H., 2017. Deformation characteristics of the Neoproterozoic Langshan Group in Langshan Region and their tectonic implications. Geological Review 5(63):1180 – 1192 (in Chinese with English abstract)

Tian, R.S., Xie, G.A., Zhang, J., Zhu, W.B., Qu, J.F., Gao, S., 2019. Sedimentary provenance and age of the Langshan Group in the northeastern Alxa Block: implications for Neoproterozoic tectonic evolution. Internal

Journal of Earth Science 108, 1705–1723.

Wang, Q., Xu, J.F., Jian, P., Bao, Z.W., Zhao, Z.H., Li, C.F., Xiong, X.L., Ma, J.L., 2006. Petrogenesis of adakitic porphyries in an extensional tectonic setting, Dexing, South China: implications for the genesis of porphyry copper mineralization. Journal of Petrology 47, 119﹣144.

Wang, B., Cluzel, D., Shu, L., Faure, M., Charvet, J., Chen, Y., Meffre, S., and de Jong, K., 2009. Evolution of calc-alkaline to alkaline magmatism through Carboniferous convergence to Permian transcurrent tectonics, western Chinese Tianshan. International Journal of Earth Sciences, 98, 1275-1298.

Wang, B., Jahn, B.M., Lo, C.H., Shu, L.S., Wu, C.Y., Li, K.S., Wang. F., 2011. Structural analysis and 40Ar /39Ar thermochronology of Proterozoic rocks in Sailimu area (NW China): Implication to polyphase tectonics of the North Chinese Tianshan. Journal of Asian Earth Sciences，42(5) : 839–853.

Wang, T., Wang, J., Liu, J., 1994. Igneous rock associations and geochemical characteristics of volcanic arc with continental crustal basement in Zongnaishan﹣Shalazhashan. Geochimica 23, 162﹣172 (in Chinese with English abstract).

Wang, T., Gao, J., Wang, J., Wu, J., 1998. Magmatism of collisional and post–orogenic period in Northern Alaxa region in Inner Mongolia. Acta Geol. Sinica 72, 126﹣136 (in Chinese with English abstract).

Wang, T., Zheng, Y., Gehrels, G., Mu, Z. 2001. Geochronological evidence for existence of South Mongolian micro–continent: a zircon U–Pb age of grantoid gneisses from the Yagan–Onch Hayrhan metamorphic core complex. Chinese Science Bulletin 46, 2005–8 (in Chinese with English abstract).

Wang, X.S., Klemd, R., Gao, J., Jiang, T., Li, J.–L., & Xue, S.C., 2018a. Final assembly of the southwestern Central Asian Orogenic Belt as constrained by the evolution of the South Tianshan Orogen: Links with Gondwana and Pangea. Journal of Geophysical Research: Solid Earth, 123, 7361﹣7388. https://doi.org/10.1029/2018JB015689

Wang, Y., Li, J.Y., Sun, G.H., 2008. Postcollisional Eastward Extrusion and Tectonic Exhumation along the Eastern Tianshan Orogen, Central Asia: Constraints from Dextral Strike–Slip Motion and 40Ar/39Ar Geochronological Evidence. The Journal of Geology 116(6):599–618.

Wang, Y., Zhou, L.Y., Zhao, L.J., 2013. Cratonic reactivation and orogeny: an example from the northern margin of the North China Craton. Gondwana Res. 24, 1203–1222.

Wang, Y., Zeng, Q., Guo, L., and Guo, Y., 2019. Magmatic and tectonic setting of the Permian Au mineralization in the Xing–Meng Orogenic Belt: constraints from the U–Pb ages, Hf–O isotopes and geochemistry of granitic intrusions in the Bilihe and Hadamiao gold deposits: Mineralogy and Petrology, 113, 99–118.

Wang, Z.H., Wan, J.L., 2014. Collision–induced Late Permian–Early Triassic transpressional deformation in the Yanshan Tectonic Belt, North China. The Journal of Geology，122(6) : 705﹣716.

Wang, Z. Z., Han, B. F., Feng, L. X., Liu, B., 2015. Geochlonology, geochemistry and origins of the Paleozoic–Triassic plutons in the Langshan area, western Inner Mongolia, China. Journal of Asian Earth Sciences, 97, 337﹣351. https://doi.org/10.1016/j.jseaes.2014.08.005

Winchester, J.A., Floyd, P.A., 1977. Geochemical discrimination of different magma series and their differentiation products using immobile elements. Chem. Geol. 20, 325﹣343.

Windley, B.F., Alexeiev, D., Xiao, W., Kröner, A., Badarch, G., 2007. Tectonic models for accretion of the Central Asian Orogenic belt. Journal of Geological Society. London. 164, 31﹣47.

Windley, B.F., Xiao, W., 2018. Ridge subduction and slab windows in the Central Asian Orogenic Belt: Tectonic implications for the evolution of an accretionary orogen. Gondwana Research 61, 73–87. https://doi.org/10.1016/j.gr.2018.05.003

Wu, T. R., He, G. Q. (1993). Tectonic units and their fundamental characteristics on the northern margin of the Alxa Block. Acta Geologica Sinica (English Edition), 6(4), 373﹣385.

Xiao, W.J., Windley, B.F., Allen, M.B., Han, C.M., 2013. Paleozoic multiple accretionary and collisional tectonics of the Chinese Tianshan orogenic collage. Gondwana Research. 23, 1316–1341.

Xiao, W.J., Windley, B.F., Sun, S., Li, J.L., Huang, B.C., Han, C.M., Yuan, C., Sun, M., Chen, H.L., 2015. A tale of amalgamation of three collage systems in the Permian– Middle Triassic in Central Asia: oroclines, sutures and terminal accretion. Annual Review of Earth Planetary Science. 43, 477–507.

Xiao, W.J., Windley, B.F., Han, C.M., Liu, W., Wan, B., Zhang, J.E., Ao, S.J., Zhang, Z.Y., Song, D.F., 2018, Late Paleozoic to early Triassic multiple roll–back and oroclinal bending of the Mongolia collage in Central Asia: Earth–Science Reviews.186, 94–128.

Xie, L., Yin, H.Q., Zhou, H.R., Zhang, W.J., 2014. Permian radiolarians from the Engeerwusu suture zone in Alxa area of Inner Mongolia and its geological significance. Geological Bulletin of China 33 (5), 691–697 (in Chinese with English abstract).

Xu, B., Charvet, J., Chen, Y., Zhao, P., Shi, G. Z., 2013. Middle Paleozoic convergent orogenic belts in western Inner Mongolia (China): framework, kinematics, geochronology and implications for tectonic evolution of the Central Asian Orogenic Belt. Gondwana Res. 23:1342–1364.

Xu, Z.Q., Li, S.T., Zhang, J.X., Yang, J.S., He, B.Z., Li, H. B., Lin, C.S., Cai, Z.H., 2011a. Paleo–Asian and Tethyan tectonic systems with docking the Tarim block. Acta Petrologica Sinica，27(1) : 1 –22 (in Chinese with English abstract).

Xu, Z.Q., Li, H.B., Tang, Z.M., Qi, X.X., Li, H.Q., Cai, Z.H., 2011b. The transformation of the terrain structures of the Tibet Plateau through large–scale strike–slip faults. Acta Petrologica Sinica, 27(11):3157–3170 (in Chinese with English abstract).

Yang, T.N., Wang, Y., Li, J.Y., Sun, G.H., 2007. Vertical and horizontal strain partitioning of the Central Tianshan (NW China): evidence from structures and 40Ar/39Ar geochronology. Journal Structural Geology 29, 1605 – 1621.

Yang, Q.D., Zhang, L., Wang, T., Shi, X.J., Zhang, J.J., Tong, Y., Guo, L., Geng, J.Z., 2014. Geochemistry and LA–ICP–MS zircon U – Pb age of Late Carboniferous Shalazhashan pluton on the northern margin of the Alxa Block, Inner Mongolia and their implications. Geological Bulletin of China 33 (6), 776 – 787 (in Chinese with English abstract).

Yin, H. Q., Zhou, H. R., Zhang, W. J., Zheng, X. M., Wang, S. Y., 2016. Late Carboniferous to early Permian sedimentary–tectonic evolution of the north of Alxa, Inner Mongolia, China: Evidence from the Amushan Formation. Geoscience Frontiers 7, 733–741.

Yuan, Y., Zong, K., Cawood, P.A., Cheng, H., Yu, Y., Guo, J., Liu, Y., Hu, Z., Zhang, W., Li, M., 2019. Implication of Mesoproterozoic (∼1.4 Ga) magmatism within microcontinents along the southern Central Asian Orogenic Belt. Precambrian Research 327, 314–326.

Zhang, S.H., Zhao, Y., Song, B., Yang, Z.Y., Hu, J.M., Wu, H., 2007a. Carboniferous granitic plutons from the northern margin of the North China block: implications for a late Palaeozoic active continental margin. J. Geol. Soc. 164, 451 – 463.

Zhang, S.H., Zhao, Y., Kröner, A., Liu, X.M., Xie, L.W., Chen, F.K., 2009a. Early Permian plutons from the northern North China Block: constraints on continental arc evolution and convergent margin magmatism related to the Central Asian Orogenic Belt. International Journal of Earth Sciences 98, 1441 – 1467.

Zhang, S.H., Zhao, Y., Song, B., Hu, J.M., Liu, S.W., Yang, Y.H., Chen, F.K., Liu, X.M., Liu, J., 2009b. Contrasting Late Carboniferous and Late Permian – Middle Triassic intrusive suites from the northern margin of the North China Craton: Geochronology, Petrogenesis and tectonic implications. Geological Society of America Bulletin 121, 181 – 200.

Zhang, J.J., Wang, T., Zhang, Z.C., Tong, Y., Zhang, L., Shi, X.J., Guo, L., Li, S., Zeng, T., 2012. Magma mixing origin of Yamatu granite in Nuoergong–Langshan area, western part of the Northern Margin of North China Craton: petrological and geochemical evidences. Geol. Rev. 58, 53–66 (in Chinese with English abstract).

Zhang, W., Wu, T.R., Feng, J.C., Zheng, R. G., He, Y.K., 2013a. Time constraints for the closing of the Paleo–Asian Ocean in the Northern Alxa Region: evidence from Wuliji granites. Science China Earth Sciences 56, 153 – 164. http://dx.doi.org/10.1007/s11430–012–4435–y.

Zhang, J.X., Gong, J.H., Yu, S.Y., Li, H.K., Hou, K.J., 2013b. Neoarchean–Paleoproterozoic multiple tectonothermal events in the western Alxa Block, NCC and their geological implication: evidence from zircon U–Pb ages and Hf isotopic composition. Precambrian Research 235, 36–57.

Zhang, J., Li, J., Xiao, W., Wang, Y., Qi, W., 2013c. Kinematics and geochronology of multistage ductile deformation along the eastern Alxa Block, NW China: new constraints on the relationship between the North China Plate and the Alxa Block. Journal of Structural Geology 57, 38–57.

Zhang, X.H., Zhang, H.F., Tang, Y.J., Wilde, S.A., Hu, Z.C., 2008. Geochemistry of Permian bimodal volcanic rocks from central Inner Mongolia, north China: implication for tectonic setting and Phanerozoic continental growth in central Asian orogenic belt. Chemical Geology 249:262 – 281

Zhang, X.R., Zhao, G.C., Eizenhöfer, P.R., Sun, M., Han, Y.G., Hou, W.Z., Liu, D.X., Wang, B., Liu, Q., and Xu, B., 2015a, Paleozoic magmatism and metamorphism in the Central Tianshan block revealed by U–Pb and Lu–Hf isotope studies of detrital zircons from the South Tianshan belt, NW China: Lithos, v. 233, p. 193–208, https://doi.org/10.1016/j.lithos.2015.06.002.

Zhang, J. J., Wang, T., Zhang, L., Tong, Y., Zhang, Z. C., Shi, X. J., et al. 2015b. Tracking deep crust by zircon xenocrysts within igneous rocks from the northern Alxa, China: Constraints on the southern boundary of the central Asian Orogenic Belt. Journal of Asian Earth Sciences, 108, 150 – 169. https://doi.org/10.1016/j.jseaes.2015.04.019

Zhang, J., Zhang, Y.P., Xiao, W.X., Wang, Y.N., 2015c. Linking the Alxa Block to the northern margin of the eastern Gondwana during the Early Paleozoic: constraints from detrital zircon U–Pb ages and sandstone composition modes of Cambrian strata. Gondwana Research. 28, 1168–1182.

Zhang, X.R., Zhao, G.C., Eizenhöfer, P.R., Sun, M., Han, Y.G., Hou, W.Z., Liu, D.X., Wang, B., Liu, Q., Xu, B., and Zhu, Y.L., 2016a, Tectonic transition from late Carboniferous subduction to Early Permian post–collisional extension in the Eastern Tianshan, NW China: Insights from geochronology and geochemistry of mafic–intermediate intrusions: Lithos, v. 256–257, p. 269–281, https://doi.org/10.1016/j .lithos.2016.04.006.

Zhang, J. J., Wang, T., Castro, A., Zhang, L., Shi, X. J., Tong, Y., Maria Iaccheri, L., 2016b. Multiple mixing and hybridization from magma source to final emplacement in the Permian Yamatu Pluton, the Northern Alxa Block, China. Journal of Petrology, 57, 933 – 980.

Zhang, X., Zhang, C., Santosh, M., Liu, L., Liu, D., and Luo, Q., 2018a, Early Silurian to Early Carboniferous ridge subduction in NW Junggar: Evidence from geochronological, geochemical, and Sr–Nd–Hf isotopic data on alkali granites and adakites: Lithos 300–301,314–329

Zhang, X., Lentz, D.R., Yao, C., Liu, R., Yang, Z., Mei, Y., Fan, X., Huang, F., Qin, Y., Zhang, K., and Zhang, Z., 2018b. Geochronology, geochemistry, and Sr–Nd–Pb–Hf isotopes of the Zhunsujihua granitoid intrusions associated with the molybdenum deposit, northern Inner Mongolia, China: implications for petrogenesis and tectonic setting: International Journal of Earth Sciences, v. 107, p. 687–710.

Zhang, L., Liu, Y.J., Shao, J., Li, W.M., Liang, C.Y., Chang, R.H., Yang, H.Z., Feng, Z.Q., Zhang, C., Xu, J., Shi, Y., Yang, F., He, P.F., 2019. Early Permian A–type Granites in the Zhangdaqi Area, Inner Mongolia, China and Their Tectonic Implications. Acta Geologica Sinica (English Edition), 93(5): 1300–1316. DOI: 10.1111/1755–6724.14385

Zheng, R.G., Wu, T.R., Zhang, W., Xu, C., Meng, Q.P., and Zhang, Z.Y., 2014, Late Paleozoic subduction system in the northern margin of the Alxa Block, Altaids: Geochronological and geochemical evidences from ophiolites: Gondwana Research, v. 25, p. 842–858, https:// doi.org/10.1016/j.gr.2013.05.011.

Zheng, R. G., Li, J. Y., Liu, J. F., 2017. The age of volcanic rocks of Amushan Formation on the northern margin of Alxa block: Evidence from zircon U–Pb data. Geology in China 44(3), 612–613 (in Chinese with English abstract).

Zheng, R. G., Zhang, J., Xiao, W, J., 2019a. Association of Permian gabbro and granite in the Langshan, southern Central Asian Orogenic Belt: Age, origin, and tectonic implications. Lithos 348–349, 105174.

Zheng, R.G., Li, J.Y., Zhang, J., Xiao, W.J., Li, Y., 2019b. Early Carboniferous High Ba‑Sr Granitoid in Southern Langshan of Northeastern Alxa: Implications for Accretionary Tectonics along Southern Central Asian Orogenic Belt. Acta Geologica Sinica (English Edition). 93, 820–844.

Zhou, Y. Z., Han, B. F., Xu, Z., Ren, R., Su, L., 2013. The age of the Proterozoic rocks in Yingba area in western Inner Mongolia: constrains on the distribution of the South Gobi micro–continent in the Central Asian Orogenic Belt. Geological Bulletin of China 32 (2–3), 318–326 (in Chinese with English abstract).

Supplementary Material for

Late Paleozoic tectonic evolution of the Paleo-Asian Ocean in the northern Alxa Block (NW China)

Rongsong Tian[1], Guoai Xie[1]*, Wenbin Zhu[1]*, Jin Zhang[2], Beihang Zhang[2] Heng Zhao[2], Shuang Gao[1], Tian Li[1]

* Corresponding author. Email: njuxie@nju.edu.cn (G.-A. Xie)
zwb@nju.edu.cn (W.-B. Zhu)

Supplementary Materials include:
Supplementary text: LA-ICP-MS Zircon U–Pb dating and whole–rock major and trace element Analytical methods
Table S1: LA-ICP-MS zircon U–Pb isotopic dating results
Table S2: whole–rock major and trace element compositions of volcanic rocks
Table S3: References of geochronological data in Langshan (Fig. 2).
Supplementary figure: Cumulative probability curves of measured crystallization ages for detrital zircons grains relative to the depositional age of samples from the Permian Dahongshan Formation.

LA-ICP-MS zircon U–Pb dating: The samples were prepared for U–Pb dating after photographing under reflected and transmitted lights. Cathodoluminescence (CL) imaging was carried out at Langfang Sincerity Geological service Co., Ltd, Hebei Province, China, to identify the internal structures and to select target points for U–Pb isotopic analyses. In situ zircon U-Pb dating were carried out at the State Key Laboratory for Mineral Deposits Research, Nanjing University, using an Agilent 7500a ICP–MS (Inductively Coupled Plasma-Mass Spectrometry) attached to a Geolas 213 nm laser ablation system with an in–house sample cell. Detailed analytical procedures are similar to those described by Griffin et al. (2004) and Jackson et al. (2004). U–Pb fractionation was corrected using zircon standard GEMOC GJ–1 ($^{207}Pb/^{206}Pb$ age of 608.5±1.5 Ma, Jackson et al., 2004) and accuracy was controlled using zircon standards 91500 ($^{207}Pb/^{206}Pb$ age of 1065.4±0.6 Ma, Wiedenbeck et al., 1995) and Mud Tank (intercept age of 732±5 Ma). All analyses were carried out using a beam with a spot size of 32μm and a repetition rate of 5 Hz. Zircon U-Pb concordia and weighted average ages diagrams were made using Isoplot (version 3.23; Ludwig, 2003).

Whole–rock major and trace element of the Permian volcanic rocks: 12 samples were used to analyze major and trace component at the ALS Laboratory Group, Guangzhou, China. Major elements were measured by X–ray fluorescence spectrometry (XRF), using fused lithium tetraborate glass pellets. Generally, major and trace-elements analytical precision is higher than 2% and 5%, respectively. Detailed analytical procedures can be found in Dai et al. (2017).

References

Griffin, W.L., Belousova, E.A., Shee, S.R., Pearson, N.J., O'Reilly, S.Y., 2004. Archean crustal evolution in the northern Yilgarn Craton: U–Pb and Hf-isotope evidence from detrital zircons. Precambrian Res. 131, 231–282.

Dai, F., Zhao, Z., and Zheng, Y., 2017. Partial melting of the orogenic lower crust: Geochemical insights from post-collisional alkaline volcanics in the Dabie orogen: Chemical Geology, v. 454, p. 25-43.

Jackson, S.E., Pearson, N.J., Griffin, W.L., Belousova, E.A., 2004. The application of laser ablation-inductively coupled plasma-mass spectrometry to in situ U–Pb zircon geochronology. Chem. Geol. 211, 47–69.

Wiedenbeck M, Alle P, Corfu F, Griffin WL, Meier M, Oberli F, von Quadt A, Roddick JC, Spiegel W (1995) Three natural zircon standards for U-Th–Pb, Lu–Hf, trace element and REE analyses. Geostand Newslett 19:1–23

Ludwig, K. R., 2003. Manual for Isoplot 3.7: Berkeley Geochronological Center Special Publication 4 (77 p.).

Table S1. LA-ICP-MS zircon U–Pb isotopic dating results from Nuoergong-Langshan Zone.

Sample	Th (ppm)	U (ppm)	Th/U	Ratio						Age (Ma)					
				$^{207}Pb/^{206}Pb$	1σ	$^{207}Pb/^{235}U$	1σ	$^{206}Pb/^{238}U$	1σ	$^{207}Pb/^{206}Pb$	1σ	$^{207}Pb/^{235}U$	1σ	$^{206}Pb/^{238}U$	1σ
19A01 (Dacite)	**Lat. N41°10′ 51″, Long. E106°20′ 19″**														
19A01-1	96	203	0.47	0.05643	0.00094	0.55209	0.00971	0.07097	0.00087	469	19	446	6	442	5
19A01-2	172	277	0.62	0.11966	0.00771	0.77661	0.04839	0.04707	0.00077	1951	118	584	28	297	5
19A01-3	154	271	0.57	0.05049	0.00101	0.29072	0.00598	0.04176	0.00052	218	26	259	5	264	3
19A01-4	123	192	0.64	0.05166	0.00123	0.29704	0.00719	0.0417	0.00053	270	33	264	6	263	3
19A01-5	146	270	0.54	0.05103	0.00143	0.29318	0.00835	0.04168	0.00051	242	43	261	7	263	3
19A01-6	81	176	0.46	0.05546	0.00131	0.54028	0.01304	0.07066	0.00088	431	32	439	9	440	5
19A01-7	126	223	0.57	0.05514	0.00118	0.53892	0.01178	0.07089	0.0009	418	27	438	8	442	5
19A01-8	102	222	0.46	0.05564	0.0011	0.54802	0.01124	0.07145	0.00089	438	25	444	7	445	5
19A01-9	91	182	0.50	0.05288	0.00207	0.30119	0.01168	0.04131	0.00061	324	61	267	9	261	4
19A01-10	66	132	0.50	0.05534	0.00109	0.54768	0.01117	0.07179	0.0009	426	24	443	7	447	5
19A01-11	97	389	0.25	0.05544	0.00116	0.54059	0.01158	0.07073	0.00089	430	26	439	8	441	5
19A01-12	88	183	0.48	0.05544	0.00098	0.54392	0.01003	0.07117	0.00088	430	21	441	7	443	5
19A01-13	64	144	0.45	0.05584	0.0017	0.54816	0.01668	0.07121	0.00097	446	43	444	11	443	6
19A01-14	85	165	0.52	0.05615	0.00102	0.54857	0.01041	0.07087	0.00088	458	22	444	7	441	5
19A01-15	106	190	0.56	0.05593	0.00115	0.55094	0.0117	0.07145	0.0009	450	26	446	8	445	5
19A01-16	236	841	0.28	0.05598	0.00098	0.54853	0.01006	0.07107	0.00088	452	20	444	7	443	5
19A01-17	87	207	0.42	0.05489	0.00124	0.53576	0.01242	0.07079	0.00087	408	30	436	8	441	5
19A01-18	82	315	0.26	0.05568	0.00083	0.548	0.00872	0.07139	0.00087	440	17	444	6	445	5
19A01-19	242	1301	0.19	0.05586	0.00066	0.54733	0.00726	0.07108	0.00085	447	13	443	5	443	5
19A01-20	402	445	0.90	0.05056	0.00089	0.29267	0.00537	0.04199	0.00052	221	21	261	4	265	3
19A01-21	95	188	0.51	0.05623	0.00102	0.55098	0.01043	0.07108	0.00088	461	21	446	7	443	5
19A01-22	81	238	0.34	0.05717	0.00096	0.55886	0.00985	0.0709	0.00087	498	19	451	6	442	5

19A01-23	98	212	0.46	0.05606	0.00092	0.54722	0.00943	0.07081	0.00087	455	19	443	6	441	5
19A01-24	169	276	0.61	0.05521	0.00114	0.54074	0.01147	0.07104	0.0009	421	26	439	8	442	5
19A01-25	106	200	0.53	0.05508	0.00166	0.53347	0.01462	0.07024	0.00087	416	69	434	10	438	5
19A01-26	118	271	0.44	0.05629	0.00091	0.55007	0.00937	0.07088	0.00087	464	18	445	6	441	5
19A01-27	134	306	0.44	0.05542	0.00085	0.54208	0.00883	0.07095	0.00086	429	17	440	6	442	5

TLS18-22 (Andesite) **Lat. N40°45′33″, Long. E106°22′06″**

TLS18-22-1	114	268	0.42	0.05377	0.00178	0.31838	0.01138	0.04295	0.00113	361	76	281	9	271	7
TLS18-22-2	77	190	0.41	0.05321	0.00204	0.31621	0.01277	0.04311	0.00116	338	89	279	10	272	7
TLS18-22-3	284	370	0.77	0.05316	0.00166	0.31472	0.01074	0.04295	0.00112	336	72	278	8	271	7
TLS18-22-4	159	249	0.64	0.05273	0.00197	0.31243	0.01235	0.04298	0.00115	317	87	276	10	271	7
TLS18-22-5	150	233	0.65	0.04996	0.00187	0.2968	0.0118	0.04309	0.00115	193	89	264	9	272	7
TLS18-22-6	113	177	0.64	0.05267	0.00284	0.30685	0.01671	0.04226	0.00122	315	126	272	13	267	8
TLS18-22-7	63	146	0.43	0.05236	0.00303	0.30948	0.01798	0.04288	0.00127	301	135	274	14	271	8
TLS18-22-8	104	238	0.44	0.05342	0.00195	0.31576	0.01225	0.04287	0.00115	347	85	279	9	271	7
TLS18-22-9	91	215	0.42	0.05061	0.00329	0.29945	0.01768	0.04291	0.00117	223	149	266	14	271	7
TLS18-22-10	123	229	0.54	0.05339	0.00195	0.31727	0.01233	0.0431	0.00116	345	85	280	10	272	7
TLS18-22-11	101	97	1.04	0.05348	0.00284	0.24885	0.01336	0.03375	0.00099	349	123	226	11	214	6
TLS18-22-12	81	190	0.43	0.05095	0.00214	0.29894	0.0132	0.04255	0.00115	239	99	266	10	269	7
TLS18-22-13	67	171	0.39	0.05266	0.00213	0.30948	0.0131	0.04263	0.00117	314	94	274	10	269	7
TLS18-22-14	152	294	0.52	0.05154	0.0019	0.30427	0.01197	0.04282	0.00115	265	87	270	9	270	7
TLS18-22-15	212	298	0.71	0.05307	0.002	0.31535	0.01262	0.0431	0.00117	332	88	278	10	272	7
TLS18-22-16	112	211	0.53	0.05179	0.00418	0.30299	0.02286	0.04243	0.0012	276	185	269	18	268	7
TLS18-22-17	97	169	0.57	0.0807	0.00227	2.22119	0.07082	0.19964	0.0053	1214	57	1188	22	1173	28
TLS18-22-18	65	156	0.42	0.05163	0.00245	0.30388	0.01497	0.04269	0.00118	269	111	269	12	269	7
TLS18-22-19	137	221	0.62	0.05539	0.00222	0.32849	0.01384	0.04301	0.00119	428	92	288	11	271	7
TLS18-22-20	81	166	0.49	0.05182	0.00215	0.30671	0.0134	0.04292	0.00118	277	97	272	10	271	7
TLS18-22-21	79	181	0.43	0.05175	0.00193	0.31063	0.01236	0.04354	0.00119	274	88	275	10	275	7
TLS18-22-22	86	120	0.72	0.05177	0.0026	0.30302	0.01555	0.04246	0.00123	275	118	269	12	268	8
TLS18-22-23	102	172	0.59	0.05154	0.00265	0.29975	0.01571	0.04218	0.00123	265	121	266	12	266	8
TLS18-22-24	97	215	0.45	0.05452	0.00763	0.31939	0.04341	0.04249	0.002	393	317	281	33	268	12
TLS18-22-25	146	240	0.61	0.05161	0.00182	0.30178	0.01151	0.04241	0.00115	268	83	268	9	268	7
TLS18-22-26	89	196	0.45	0.05111	0.00213	0.3021	0.01327	0.04287	0.00119	246	98	268	10	271	7
TLS18-22-27	40	238	0.17	0.07055	0.00199	1.44375	0.04649	0.14843	0.00397	944	59	907	19	892	22
TLS18-22-28	139	235	0.59	0.05022	0.00257	0.29706	0.01557	0.04291	0.00124	205	119	264	12	271	8
TLS18-22-29	141	243	0.58	0.051	0.00213	0.2989	0.01317	0.04251	0.00118	241	99	266	10	268	7
TLS18-22-30	126	277	0.45	0.05161	0.00477	0.30587	0.02665	0.04299	0.00133	268	212	271	21	271	8

19A12 (Rhyolite) **Lat. N40°01′31″, Long. E105°11′39″**

19A12-1	110	123	0.89	0.0553	0.00258	0.32829	0.01513	0.04306	0.00071	424	73	288	12	272	4
19A12-2	195	239	0.81	0.05274	0.00159	0.31184	0.00953	0.04289	0.00059	318	45	276	7	271	4
19A12-3	358	254	1.41	0.05204	0.00104	0.31174	0.00655	0.04345	0.00057	287	25	276	5	274	4
19A12-4	188	216	0.87	0.05177	0.00132	0.31102	0.00809	0.04357	0.00059	275	35	275	6	275	4
19A12-5	153	130	1.17	0.168	0.00208	11.01619	0.15793	0.47565	0.0061	2538	11	2525	13	2508	27

19A12-6	215	218	0.99	0.0525	0.00146	0.31179	0.0088	0.04308	0.0006	307	39	276	7	272	4
19A12-7	219	182	1.20	0.05323	0.00163	0.31539	0.00976	0.04298	0.00061	339	44	278	8	271	4
19A12-8	136	131	1.03	0.05224	0.00134	0.31119	0.00816	0.04321	0.00059	296	35	275	6	273	4
19A12-9	335	171	1.96	0.05386	0.00173	0.37844	0.01218	0.05097	0.00074	365	46	326	9	320	5
19A12-10	150	143	1.05	0.05339	0.00181	0.31731	0.01077	0.04311	0.00063	345	50	280	8	272	4
19A12-11	172	157	1.09	0.05145	0.00117	0.30967	0.00724	0.04366	0.00058	261	30	274	6	275	4
19A12-12	292	241	1.21	0.05248	0.00101	0.34681	0.00699	0.04793	0.00062	306	24	302	5	302	4
19A12-13	297	256	1.16	0.05254	0.00153	0.31069	0.00913	0.0429	0.00059	309	42	275	7	271	4
19A12-14	175	172	1.02	0.05296	0.00155	0.3161	0.00935	0.04329	0.00061	327	42	279	7	273	4
19A12-15	184	182	1.01	0.05326	0.00151	0.31443	0.00901	0.04282	0.00059	340	40	278	7	270	4
19A12-16	76	112	0.67	0.07202	0.0014	1.72603	0.03527	0.17383	0.00231	987	21	1018	13	1033	13
19A12-17	131	164	0.80	0.05346	0.00168	0.31609	0.00996	0.04289	0.00061	348	46	279	8	271	4
19A12-18	254	251	1.01	0.05135	0.00111	0.30607	0.00686	0.04323	0.00056	257	29	271	5	273	3
19A12-19	139	206	0.68	0.05208	0.00141	0.31026	0.0085	0.04321	0.00059	289	38	274	7	273	4
19A12-20	134	155	0.87	0.05284	0.00229	0.31169	0.0134	0.04278	0.00068	322	69	275	10	270	4
19A12-21	167	158	1.06	0.05239	0.00143	0.31476	0.00866	0.04358	0.0006	302	38	278	7	275	4
19A12-22	320	284	1.13	0.05205	0.00144	0.30862	0.00868	0.04301	0.00058	288	40	273	7	271	4
19A12-23	712	371	1.92	0.04997	0.00093	0.30524	0.00596	0.04431	0.00057	194	23	270	5	279	4
19A12-24	370	187	1.98	0.05163	0.00115	0.31078	0.00715	0.04366	0.00058	269	29	275	6	275	4
19A12-25	243	257	0.94	0.0507	0.00546	0.29699	0.03132	0.04249	0.00117	227	186	264	25	268	7
19A12-26	1248	636	1.96	0.05179	0.00099	0.31283	0.00624	0.04381	0.00057	276	23	276	5	276	4
19A12-27	206	350	0.59	0.05225	0.00096	0.34906	0.00674	0.04845	0.00062	296	22	304	5	305	4
19A12-28	197	156	1.27	0.04942	0.00181	0.29783	0.01088	0.04371	0.00064	168	58	265	9	276	4

TLS18-20 (Granitic mylonite)   Lat. N40°42′54″, Long. E106°22′12″

TLS18-20-1	304	315	0.97	0.05243	0.00165	0.31419	0.01102	0.04347	0.00118	304	73	277	9	274	7
TLS18-20-2	522	798	0.65	0.05045	0.00133	0.30519	0.00942	0.04388	0.00117	216	62	270	7	277	7
TLS18-20-3	307	506	0.61	0.05232	0.00159	0.31108	0.01065	0.04313	0.00116	299	71	275	8	272	7
TLS18-20-4	443	485	0.91	0.05441	0.00165	0.32108	0.01094	0.0428	0.00115	388	70	283	8	270	7
TLS18-20-5	522	580	0.90	0.05318	0.00151	0.31585	0.01024	0.04308	0.00115	336	66	279	8	272	7
TLS18-20-6	290	413	0.70	0.05137	0.00248	0.30281	0.01506	0.04275	0.00123	257	113	269	12	270	8
TLS18-20-7	197	261	0.75	0.05345	0.00187	0.31534	0.012	0.0428	0.00117	348	81	278	9	270	7
TLS18-20-8	455	656	0.69	0.05329	0.0017	0.31561	0.01118	0.04296	0.00116	341	74	279	9	271	7
TLS18-20-9	333	376	0.89	0.05205	0.00161	0.307	0.0106	0.04278	0.00115	288	72	272	8	270	7
TLS18-20-10	445	871	0.51	0.05184	0.00136	0.30583	0.00942	0.04279	0.00114	278	61	271	7	270	7
TLS18-20-12	519	827	0.63	0.05295	0.0014	0.31605	0.00974	0.0433	0.00115	327	61	279	8	273	7
TLS18-20-13	161	161	1.00	0.05294	0.00188	0.32177	0.01234	0.04409	0.00121	326	83	283	9	278	7
TLS18-20-14	416	484	0.86	0.05341	0.00171	0.31625	0.01122	0.04295	0.00116	346	74	279	9	271	7
TLS18-20-15	357	322	1.11	0.05235	0.00168	0.31355	0.01117	0.04345	0.00117	301	75	277	9	274	7
TLS18-20-16	304	352	0.86	0.05228	0.00236	0.31099	0.01456	0.04315	0.00122	298	106	275	11	272	8
TLS18-20-17	128	109	1.17	0.0517	0.003	0.30737	0.01797	0.04313	0.0013	272	135	272	14	272	8
TLS18-20-18	284	323	0.88	0.05278	0.00173	0.31452	0.01134	0.04323	0.00117	319	76	278	9	273	7

TLS18-21 (Undeformed diorite veins)   Lat. N40°44′20″, Long. E106°21′57″

TLS18-21-1	243	371	0.65	0.05658	0.00822	0.30152	0.04248	0.03866	0.00186	474	293	268	33	245	12
TLS18-21-2	558	2626	0.21	0.05125	0.00133	0.31623	0.00975	0.04477	0.00119	252	61	279	8	282	7
TLS18-21-3	179	179	1.00	0.05733	0.00184	0.62973	0.02246	0.07969	0.00216	504	72	496	14	494	13
TLS18-21-4	278	290	0.96	0.05415	0.00203	0.29669	0.01187	0.03974	0.00104	377	86	264	9	251	6
TLS18-21-5	237	164	1.44	0.0561	0.00187	0.57827	0.02129	0.07479	0.00203	456	76	463	14	465	12
TLS18-21-6	704	1856	0.38	0.05413	0.00152	0.35159	0.01134	0.04713	0.00126	376	65	306	9	297	8
TLS18-21-7	92	97	0.94	0.0524	0.00251	0.28664	0.01442	0.03968	0.00111	303	112	256	11	251	7
TLS18-21-8	287	404	0.71	0.05291	0.00162	0.33415	0.01146	0.04582	0.00123	325	71	293	9	289	8
TLS18-21-9	722	616	1.17	0.0537	0.00162	0.32268	0.01092	0.0436	0.00116	358	70	284	8	275	7
TLS18-21-10	156	289	0.54	0.05449	0.00187	0.34096	0.01278	0.0454	0.00122	391	79	298	10	286	8
TLS18-21-11	564	420	1.34	0.05231	0.00206	0.29014	0.01203	0.04023	0.00106	299	92	259	9	254	7
TLS18-21-12	306	354	0.87	0.05292	0.00153	0.28869	0.00931	0.03957	0.00103	325	67	258	7	250	6
TLS18-21-13	54	56	0.95	0.16147	0.00402	12.61392	0.37185	0.5668	0.01502	2471	43	2651	28	2895	62
TLS18-21-14	71	72	0.98	0.1656	0.0041	11.07561	0.3243	0.48526	0.01281	2514	43	2530	27	2550	56
TLS18-21-15	522	1992	0.26	0.0521	0.00129	0.38486	0.01126	0.05359	0.0014	290	58	331	8	337	9
TLS18-21-16	122	120	1.01	0.05055	0.00435	0.27931	0.02404	0.04008	0.00131	220	196	250	19	253	8
TLS18-21-17	530	2044	0.26	0.05237	0.0013	0.36128	0.01056	0.05005	0.0013	302	58	313	8	315	8
TLS18-21-18	122	181	0.68	0.06373	0.0107	0.31521	0.05199	0.03587	0.00113	733	375	278	40	227	7
TLS18-21-19	173	220	0.79	0.05466	0.00263	0.2999	0.01476	0.0398	0.00112	398	111	266	12	252	7
TLS18-21-20	425	269	1.58	0.05126	0.0035	0.283	0.01957	0.04004	0.00122	253	158	253	15	253	8
TLS18-21-21	180	529	0.34	0.06187	0.00171	0.79223	0.0246	0.09289	0.00241	670	61	592	14	573	14
TLS18-21-22	416	522	0.80	0.04759	0.00366	0.25498	0.0195	0.03886	0.00124	78	174	231	16	246	8
TLS18-21-23	560	762	0.74	0.06568	0.00182	0.48513	0.01507	0.05358	0.00139	796	59	402	10	336	9
TLS18-21-24	288	341	0.84	0.05392	0.0018	0.37678	0.01356	0.05068	0.00133	368	77	325	10	319	8
TLS18-21-25	130	153	0.85	0.05379	0.00208	0.39298	0.01589	0.05299	0.00142	362	89	337	12	333	9
TLS18-21-26	126	94	1.34	0.05004	0.00343	0.27504	0.0189	0.03987	0.00126	197	157	247	15	252	8
TLS18-21-27	98	125	0.78	0.05459	0.0024	0.41375	0.01879	0.05497	0.00149	395	101	352	13	345	9
TLS18-21-28	576	720	0.80	0.05362	0.00162	0.31881	0.01051	0.04312	0.00111	355	70	281	8	272	7
TLS18-21-29	90	141	0.64	0.05243	0.00278	0.28709	0.01573	0.03972	0.00114	304	124	256	12	251	7
TLS18-21-30	617	832	0.74	0.05475	0.0016	0.32071	0.01026	0.04248	0.00109	402	67	282	8	268	7
TLS18-21-31	43	33	1.31	0.05661	0.00581	0.32293	0.03263	0.04136	0.00141	476	234	284	25	261	9
TLS18-21-32	75	49	1.54	0.0456	0.00453	0.27545	0.02722	0.0438	0.00135	-23	204	247	22	276	8
TLS18-21-33	131	197	0.66	0.05103	0.00182	0.26042	0.00997	0.03702	0.001	242	80	235	8	234	6
TLS18-21-34	310	1775	0.17	0.05097	0.00146	0.29777	0.00932	0.04236	0.00108	239	68	265	7	267	7
TLS18-21-35	230	72	3.18	0.05242	0.00293	0.2848	0.01617	0.03941	0.00118	304	131	254	13	249	7

TLS18-23 (Granitic mylonite) Lat. N40°39′12″, Long. E106°17′24″

TLS18-23-1	289	151	1.91	0.05237	0.00207	0.31003	0.01295	0.04294	0.00119	302	92	274	10	271	7
TLS18-23-2	208	336	0.62	0.05178	0.00164	0.31002	0.01089	0.04343	0.00117	276	74	274	8	274	7
TLS18-23-3	349	382	0.91	0.0514	0.00367	0.31326	0.02224	0.04421	0.00142	259	165	277	17	279	9
TLS18-23-4	466	716	0.65	0.05158	0.0018	0.30542	0.01157	0.04295	0.00117	267	82	271	9	271	7
TLS18-23-5	535	952	0.56	0.05321	0.00158	0.31574	0.01053	0.04304	0.00115	338	69	279	8	272	7
TLS18-23-6	218	254	0.86	0.05094	0.00177	0.31042	0.01172	0.0442	0.0012	238	82	275	9	279	7
TLS18-23-7	242	194	1.25	0.05217	0.00298	0.30756	0.01777	0.04277	0.00128	293	133	272	14	270	8

TLS18-23-8	82	69	1.18	0.05418	0.00338	0.31834	0.0201	0.04262	0.00125	379	144	281	15	269	8
TLS18-23-9	85	105	0.81	0.05188	0.00267	0.30726	0.01615	0.04296	0.00125	280	121	272	13	271	8
TLS18-23-10	168	149	1.12	0.05269	0.00234	0.31308	0.01452	0.04311	0.00119	315	104	277	11	272	7
TLS18-23-11	182	158	1.15	0.05305	0.00212	0.31454	0.01326	0.04301	0.00119	331	93	278	10	271	7
TLS18-23-12	596	886	0.67	0.05267	0.00163	0.31073	0.01066	0.04279	0.00114	315	72	275	8	270	7
TLS18-23-13	79	140	0.57	0.05141	0.00209	0.30413	0.01328	0.04291	0.00118	259	96	270	10	271	7
TLS18-23-14	177	215	0.82	0.05252	0.0017	0.3101	0.01095	0.04282	0.0011	308	75	274	8	270	7
TLS18-23-15	128	118	1.09	0.05477	0.00482	0.32595	0.0284	0.04317	0.0014	403	202	286	22	272	9
TLS18-23-16	94	52	1.81	0.05398	0.00319	0.32067	0.01917	0.04309	0.00131	370	137	282	15	272	8
19A03 (Sandstone)	**Lat. N40°57′45″, Long. E106°43′54″**														
19A03-1	147	331	0.44	0.11214	0.00258	4.61326	0.09079	0.29837	0.00358	1834	43	1752	16	1683	18
19A03-2	96	321	0.30	0.06719	0.00365	1.29158	0.06887	0.13943	0.0026	844	80	842	31	841	15
19A03-3	54	94	0.57	0.08473	0.00171	2.61323	0.05328	0.22371	0.00279	1309	21	1304	15	1301	15
19A03-4	55	88	0.63	0.08457	0.00135	2.6105	0.04296	0.22389	0.00264	1306	15	1304	12	1302	14
19A03-5	61	97	0.63	0.08499	0.00125	2.62748	0.04033	0.22422	0.00261	1315	14	1308	11	1304	14
19A03-6	0	0	1.18	0.08805	0.175	3.04389	5.96675	0.25073	0.13561	1384	2821	1419	1498	1442	699
19A03-7	268	145	1.85	0.05238	0.00247	0.31573	0.01462	0.04372	0.00068	302	77	279	11	276	4
19A03-8	59	131	0.45	0.08639	0.00115	2.82316	0.03971	0.23702	0.00273	1347	12	1362	11	1371	14
19A03-9	101	74	1.37	0.05132	0.01137	0.32835	0.07111	0.04641	0.00241	255	346	288	54	292	15
19A03-10	34	87	0.39	0.12227	0.00162	6.10261	0.08633	0.36199	0.00423	1990	11	1991	12	1992	20
19A03-11	163	88	1.85	0.0528	0.0121	0.32323	0.07236	0.0444	0.00241	320	360	284		280	15
19A03-12	73	133	0.55	0.09577	0.00399	3.21567	0.13189	0.24352	0.00444	1543	50	1461	32	1405	23
19A03-13	81	47	1.73	0.05314	0.00311	0.36634	0.0211	0.04999	0.00086	335	99	317	16	314	5
19A03-14	64	98	0.65	0.0853	0.0013	2.65957	0.04254	0.22612	0.0027	1322	15	1317	12	1314	14
19A03-15	186	203	0.92	0.10874	0.00156	4.72822	0.0718	0.31535	0.00376	1778	13	1772	13	1767	18
19A03-16	89	224	0.40	0.16269	0.00211	10.50514	0.14816	0.4683	0.00555	2484	11	2480	13	2476	24
19A03-17	103	60	1.72	0.05276	0.00226	0.35582	0.01505	0.04891	0.00074	318	68	309	11	308	5
19A03-18	102	68	1.50	0.0497	0.01514	0.29534	0.08799	0.0431	0.00302	181	417	263	69	272	19
19A03-19	89	142	0.62	0.05243	0.00177	0.32777	0.01102	0.04534	0.00063	304	51	288	8	286	4
19A03-20	161	113	1.42	0.05213	0.00203	0.33529	0.01297	0.04665	0.00067	291	62	294	10	294	4
19A03-21	201	251	0.80	0.0538	0.00282	0.31007	0.01598	0.0418	0.0007	363	86	274	12	264	4
19A03-22	134	162	0.83	0.05246	0.00523	0.32265	0.03145	0.04461	0.00116	306	173	284	24	281	7
19A03-23	200	121	1.65	0.05264	0.00258	0.36115	0.01744	0.04976	0.0008	313	80	313	13	313	5
19A03-24	89	143	0.62	0.08566	0.00131	2.72564	0.04484	0.2308	0.00283	1331	15	1335	12	1339	15
19A03-25	187	202	0.93	0.05512	0.00461	0.17053	0.01395	0.02244	0.00051	417	143	160	12	143	3
19A03-26	28	24	1.18	0.05236	0.00845	0.34271	0.0541	0.04748	0.00187	301	279	299	41	299	12
19A03-27	215	271	0.79	0.11412	0.0016	5.22827	0.08088	0.33231	0.00406	1866	13	1857	13	1850	20
19A03-28	72	110	0.66	0.08571	0.00139	2.76691	0.04829	0.23416	0.00293	1332	16	1347	13	1356	15
19A03-29	53	36	1.46	0.05446	0.00318	0.37889	0.02196	0.05047	0.00081	390	101	326	16	317	5
19A03-30	164	126	1.30	0.05453	0.00675	0.3394	0.04104	0.04515	0.00142	393	214	297	31	285	9
19A03-31	58	98	0.59	0.08661	0.00134	2.7601	0.04555	0.23114	0.00287	1352	15	1345	12	1340	15
19A03-32	76	174	0.43	0.08738	0.00116	2.97204	0.04306	0.2467	0.00299	1369	13	1400	11	1421	15
19A03-33	167	101	1.66	0.05175	0.00748	0.33431	0.04726	0.04685	0.00166	274	253	293	36	295	10

19A03-34	45	99	0.46	0.09611	0.0014	3.6002	0.05637	0.27171	0.00335	1550	14	1550	12	1549	17
19A03-35	102	73	1.39	0.05193	0.00176	0.34867	0.01182	0.0487	0.00066	282	53	304	9	307	4
19A03-36	74	111	0.67	0.08645	0.00125	2.69706	0.04192	0.2263	0.00278	1348	14	1328	12	1315	15
19A03-37	67	98	0.68	0.08668	0.00122	2.85771	0.04355	0.23914	0.00293	1353	13	1371	11	1382	15
19A03-38	194	106	1.83	0.05272	0.00393	0.32299	0.02359	0.04444	0.00092	317	128	284	18	280	6
19A03-39	69	97	0.71	0.086	0.00126	2.71697	0.0427	0.22915	0.00282	1338	14	1333	12	1330	15
19A03-40	87	121	0.72	0.09045	0.00133	3.0671	0.04848	0.24595	0.00304	1435	14	1425	12	1418	16
19A03-41	88	66	1.34	0.05293	0.00356	0.35789	0.02363	0.04904	0.00096	326	115	311	18	309	6
19A03-42	192	110	1.74	0.05298	0.00221	0.36316	0.01502	0.04972	0.00076	328	66	315	11	313	5
19A03-43	65	98	0.67	0.08658	0.00126	2.75042	0.04324	0.23042	0.00284	1351	14	1342	12	1337	15
19A03-44	72	84	0.85	0.09406	0.00609	2.86415	0.17566	0.22086	0.00459	1509	126	1373	46	1286	24
19A03-45	130	146	0.89	0.05171	0.00123	0.29386	0.00709	0.04122	0.00053	273	32	262	6	260	3
19A03-46	84	119	0.70	0.08239	0.00261	2.51799	0.07297	0.22166	0.00283	1255	63	1277	21	1291	15
19A03-47	157	103	1.53	0.05183	0.00366	0.34575	0.024	0.04839	0.00097	278	122	302	18	305	6
19A03-48	304	142	2.13	0.05266	0.00281	0.34956	0.01834	0.04815	0.00082	314	88	304	14	303	5
19A03-49	56	105	0.54	0.08711	0.00131	2.77764	0.04484	0.23129	0.00286	1363	15	1350	12	1341	15
19A03-50	74	109	0.68	0.08723	0.00152	2.78475	0.05107	0.23157	0.00296	1366	17	1351	14	1343	15
19A03-51	79	105	0.75	0.09962	0.00143	3.85902	0.06002	0.281	0.00347	1617	13	1605	13	1596	17
19A03-52	47	83	0.57	0.08781	0.00137	2.79321	0.04666	0.23075	0.00288	1378	15	1354	12	1338	15
19A03-53	125	77	1.62	0.05351	0.00186	0.37619	0.01299	0.05099	0.00073	350	52	324	10	321	4
19A03-54	102	122	0.83	0.05532	0.00187	0.5223	0.01767	0.06849	0.00097	425	50	427	12	427	6
19A03-55	112	155	0.72	0.08613	0.00126	2.71424	0.04298	0.22858	0.00282	1341	14	1332	12	1327	15
19A03-56	346	235	1.47	0.05296	0.00223	0.35274	0.0147	0.04831	0.00074	327	67	307	11	304	5
19A03-57	215	98	2.19	0.05262	0.00478	0.35564	0.03167	0.04902	0.00118	312	158	309	24	309	7
19A03-58	165	93	1.78	0.06686	0.00913	0.41637	0.0563	0.04517	0.00086	833	301	353	40	285	5
19A03-59	85	125	0.68	0.08935	0.00147	2.96868	0.05202	0.24101	0.00305	1412	16	1400	13	1392	16
19A03-60	410	360	1.14	0.05656	0.00239	0.35725	0.01491	0.04582	0.00071	474	65	310	11	289	4
19A03-61	181	123	1.46	0.05578	0.00228	0.35599	0.01442	0.04629	0.00071	444	63	309	11	292	4
19A03-62	134	95	1.41	0.05277	0.00263	0.3499	0.01724	0.0481	0.00077	319	83	305	13	303	5
19A03-63	98	71	1.39	0.07197	0.01052	0.40671	0.05857	0.04098	0.00103	985	317	347	42	259	6
19A03-64	67	146	0.46	0.08769	0.00135	2.97475	0.04938	0.24609	0.00307	1376	15	1401	13	1418	16
19A03-65	96	142	0.68	0.08663	0.00135	2.74997	0.04529	0.23026	0.00285	1352	15	1342	12	1336	15
19A03-66	42	55	0.76	0.08991	0.00193	3.02462	0.06631	0.24402	0.00327	1424	22	1414	17	1408	17
19A03-67	13	408	0.03	0.05569	0.00079	0.60608	0.00927	0.07894	0.00095	440	16	481	6	490	6
19A03-68	97	204	0.48	0.16161	0.0019	10.43583	0.13743	0.46837	0.00561	2473	10	2474	12	2476	25
19A03-69	37	69	0.54	0.09902	0.00867	3.76962	0.32291	0.27614	0.00939	1606	109	1586	69	1572	47
19A03-70	189	89	2.12	0.05952	0.00566	0.38066	0.0357	0.04639	0.00073	586	214	328	26	292	5
19A03-71	66	96	0.68	0.0861	0.00137	2.69818	0.04561	0.2273	0.00284	1340	16	1328	13	1320	15
19A03-72	74	114	0.65	0.08609	0.0013	2.71586	0.04383	0.22883	0.00283	1340	15	1333	12	1328	15
19A03-73	115	73	1.58	0.05245	0.00286	0.34453	0.01876	0.04764	0.00068	305	98	301	14	300	4
19A03-74	203	126	1.61	0.05318	0.00202	0.33308	0.01252	0.04543	0.00067	336	58	292	10	286	4
19A03-75	126	91	1.39	0.05364	0.01069	0.31701	0.06165	0.04287	0.00208	356	327	280	48	271	13
19A03-76	220	305	0.72	0.09881	0.00316	3.47483	0.10121	0.25504	0.00334	1602	61	1522	23	1464	17
19A03-77	267	173	1.55	0.05114	0.00404	0.31956	0.02474	0.04532	0.00098	247	136	282	19	286	6

19A03-78	98	65	1.51	0.05291	0.00454	0.36042	0.03028	0.04941	0.00115	325	149	313	23	311	7
19A03-79	61	335	0.18	0.10704	0.00407	4.60307	0.17381	0.31193	0.00577	1750	42	1750	31	1750	28
19A03-80	71	108	0.66	0.08645	0.00133	2.69204	0.04449	0.22588	0.00283	1348	15	1326	12	1313	15
19A03-81	474	170	2.79	0.05522	0.00149	0.38506	0.01048	0.05058	0.00068	421	37	331	8	318	4
19A03-82	70	106	0.66	0.08803	0.00303	2.77132	0.09501	0.22836	0.00373	1383	41	1348	26	1326	20
19A03-83	274	174	1.57	0.05296	0.00171	0.33537	0.01084	0.04593	0.00064	327	48	294	8	289	4
19A03-84	251	146	1.72	0.05129	0.0079	0.32542	0.049	0.04603	0.00173	254	266	286	38	290	11
19A03-85	183	91	2.02	0.05596	0.00912	0.39212	0.0624	0.05083	0.00209	451	281	336	46	320	13
19A03-86	109	70	1.57	0.05248	0.00596	0.3498	0.03935	0.04834	0.00078	306	260	305	30	304	5
19A03-87	71	94	0.75		0.00249	2.78344	0.07992	0.23112	0.00347	1368	33	1351	21	1340	18
19A03-88	254	147	1.73	0.05223	0.00296	0.33808	0.0189	0.04695	0.00083	295	95	296	14	296	5
19A03-90	37	67	0.54	0.14116	0.00425	8.24192	0.22062	0.42347	0.00582	2241	53	2258	24	2276	26
19A03-91	73	108	0.68	0.0901	0.00136	2.92089	0.04814	0.23516	0.00298	1428	15	1387	12	1361	16
19A03-92	247	240	1.03	0.0553	0.00127	0.37452	0.00884	0.04913	0.00065	424	30	323	7	309	4
19A03-93	234	245	0.95	0.05545	0.0038	0.36775	0.02472	0.04811	0.00098	430	114	318	18	303	6
19A03-94	146	162	0.90	0.12556	0.00194	5.23336	0.08811	0.30237	0.00388	2037	14	1858	14	1703	19
19A03-95	228	145	1.56	0.05722	0.0081	0.36321	0.05026	0.04605	0.00161	500	245	315	37	290	10
19A03-96	75	64	1.16	0.07002	0.00754	0.4979	0.05285	0.05158	0.00094	929	231	410	36	324	6
19A03-97	60	98	0.61	0.0848	0.00139	2.72603	0.04847	0.23321	0.00301	1311	17	1336	13	1351	16
19A03-98	83	139	0.60	0.08893	0.00151	2.95074	0.05396	0.24072	0.00313	1403	17	1395	14	1390	16
19A03-99	68	133	0.51	0.09004	0.00184	3.03501	0.06498	0.24453	0.00332	1426	21	1416	16	1410	17

19A04 (Sandstone) Lat. N40°57′46″, Long. E106°43′54″

19A04-1	58	41	1.40	0.16911	0.00223	11.39856	0.16416	0.48892	0.00602	2549	11	2556	13	2566	26
19A04-2	12	12	1.07	0.15308	0.00506	9.93314	0.33072	0.47068	0.00872	2381	32	2429	31	2487	38
19A04-3	71	200	0.35	0.1483	0.00184	8.33331	0.11399	0.4076	0.0049	2326	10	2268	12	2204	22
19A04-4	137	120	1.14	0.15441	0.0047	9.42537	0.28805	0.44277	0.00803	2395	28	2380	28	2363	36
19A04-5	31	199	0.15	0.11788	0.00144	5.82576	0.07843	0.35847	0.00426	1924	11	1950	12	1975	20
19A04-6	252	745	0.34	0.05648	0.00076	0.56542	0.00823	0.07261	0.00086	471	15	455	5	452	5
19A04-7	36	113	0.32	0.12844	0.00286	6.55331	0.12039	0.37004	0.00468	2077	40	2053	16	2030	22
19A04-8	42	55	0.75	0.1713	0.00465	10.65214	0.25095	0.45101	0.00607	2570	46	2493	22	2400	27
19A04-9	15	58	0.26	0.12087	0.00169	5.91526	0.08879	0.35498	0.00431	1969	12	1963	13	1958	21
19A04-10	37	73	0.51	0.11626	0.00161	5.5807	0.08316	0.34817	0.00421	1899	12	1913	13	1926	20
19A04-11	53	102	0.52	0.11586	0.0016	5.42538	0.0806	0.33967	0.00409	1893	12	1889	13	1885	20
19A04-12	125	155	0.81	0.11469	0.00155	5.37081	0.07809	0.33968	0.00406	1875	12	1880	12	1885	20
19A04-13	36	53	0.68	0.11703	0.00175	5.65614	0.08964	0.35056	0.00429	1911	13	1925	14	1937	20
19A04-14	38	45	0.83	0.0559	0.00307	0.38838	0.02107	0.0504	0.00083	448	91	333	15	317	5
19A04-15	55	149	0.37	0.1148	0.00163	5.35594	0.08116	0.33842	0.00406	1877	13	1878	13	1879	20
19A04-16	79	200	0.39	0.11863	0.00285	5.52859	0.11169	0.33801	0.00438	1936	44	1905	17	1877	21
19A04-17	119	98	1.21	0.05409	0.00407	0.37294	0.02745	0.05001	0.00106	375	128	322	20	315	7
19A04-18	82	141	0.58	0.11807	0.00253	5.56364	0.09854	0.34177	0.00413	1927	39	1910	15	1895	20
19A04-19	179	103	1.73	0.10849	0.00174	4.54238	0.07656	0.3037	0.00379	1774	15	1739	14	1710	19
19A04-20	68	141	0.48	0.11968	0.00155	5.69734	0.08019	0.34531	0.00412	1951	11	1931	12	1912	20
19A04-22	135	177	0.77	0.11368	0.00174	5.18595	0.08411	0.3309	0.0041	1859	14	1850	14	1843	20

19A04-23	236	198	1.19	0.16587	0.00212	10.90993	0.15254	0.47711	0.0057	2516	11	2515	13	2515	25
19A04-24	89	247	0.36	0.11664	0.00168	5.49316	0.08477	0.34162	0.00417	1905	13	1900	13	1894	20
19A04-25	147	85	1.73	0.09862	0.00146	3.75741	0.05935	0.27636	0.00337	1598	14	1584	13	1573	17
19A04-26	87	102	0.85	0.05551	0.00152	0.50731	0.01391	0.06629	0.00088	433	38	417	9	414	5
19A04-27	86	114	0.76	0.15675	0.00257	9.76616	0.1688	0.45193	0.00581	2421	14	2413	16	2404	26
19A04-28	171	195	0.88	0.12351	0.00191	6.32116	0.10375	0.37124	0.0046	2008	14	2021	14	2035	22
19A04-29	79	83	0.96	0.16728	0.00262	10.94112	0.18216	0.47442	0.00598	2531	13	2518	15	2503	26
19A04-30	45	56	0.80	0.15312	0.00315	9.07943	0.19258	0.43011	0.00603	2381	18	2346	19	2306	27
19A04-31	72	93	0.78	0.11457	0.00158	5.31626	0.07964	0.3366	0.00412	1873	12	1871	13	1870	20
19A04-32	50	128	0.39	0.11951	0.00165	5.78499	0.08679	0.35114	0.00431	1949	12	1944	13	1940	21
19A04-33	16	145	0.11	0.10338	0.00202	4.26806	0.08628	0.29949	0.00387	1686	19	1687	17	1689	19
19A04-34	939	745	1.26	0.05229	0.00087	0.31215	0.00548	0.04331	0.00053	298	20	276	4	273	3
19A04-35	41	158	0.26	0.12168	0.00405	5.86938	0.19476	0.34991	0.00617	1981	35	1957	29	1934	29
19A04-36	148	235	0.63	0.11987	0.00163	5.82175	0.08649	0.35232	0.00432	1954	12	1950	13	1946	21
19A04-37	329	321	1.03	0.05388	0.00113	0.39484	0.0085	0.05316	0.00068	366	26	338	6	334	4
19A04-38	136	109	1.26	0.16399	0.00227	10.7542	0.16308	0.47572	0.0059	2497	12	2502	14	2509	26
19A04-39	258	309	0.83	0.05306	0.0011	0.37155	0.00798	0.0508	0.00065	331	26	321	6	319	4
19A04-40	84	238	0.35	0.16123	0.00529	10.09653	0.33264	0.45426	0.00875	2469	31	2444	30	2414	39
19A04-41	13	49	0.26	-0.02216	0.0033	-0.93029	0.13859	0.30455	0.00412	-248	93	-2704	2019	1714	20
19A04-42	64	120	0.54	0.11882	0.00189	5.72771	0.0979	0.34969	0.00444	1939	15	1936	15	1933	21
19A04-43	243	142	1.71	0.12017	0.00179	5.87602	0.09507	0.3547	0.00443	1959	13	1958	14	1957	21
19A04-44	213	226	0.94	0.053	0.00132	0.37245	0.00947	0.05098	0.00067	329	34	321	7	321	4
19A04-45	214	281	0.76	0.11542	0.00176	5.37505	0.08902	0.3378	0.00423	1886	14	1881	14	1876	20
19A04-46	145	195	0.75	0.14537	0.00182	6.88344	0.09833	0.34346	0.00431	2292	11	2097	13	1903	21
19A04-47	57	84	0.68	0.16046	0.00205	10.25297	0.1485	0.46349	0.00585	2461	11	2458	13	2455	26
19A04-48	86	95	0.91	0.15729	0.00199	9.86643	0.14206	0.45501	0.00573	2427	11	2422	13	2417	25
19A04-49	33	208	0.16	0.11869	0.00147	5.71239	0.08089	0.34911	0.00436	1937	11	1933	12	1930	21
19A04-50	93	58	1.60	0.12216	0.00176	6.19495	0.09874	0.36784	0.00473	1988	13	2004	14	2019	22
19A04-51	562	775	0.72	0.12706	0.00575	0.75543	0.03216	0.04312	0.00066	2058	82	571	19	272	4
19A04-52	465	295	1.58	0.16618	0.00206	10.856	0.15456	0.47386	0.00593	2520	11	2511	13	2500	26
19A04-53	100	153	0.66	0.11806	0.00154	5.61377	0.08289	0.3449	0.00434	1927	12	1918	13	1910	21
19A04-54	72	45	1.61	0.16399	0.00233	10.97591	0.17357	0.48549	0.00629	2497	12	2521	15	2551	27
19A04-55	117	158	0.74	0.13523	0.00178	7.32857	0.10929	0.3931	0.00496	2167	12	2152	13	2137	23
19A04-56	479	455	1.05	0.05437	0.00086	0.37836	0.00651	0.05048	0.00064	386	18	326	5	317	4
19A04-57	148	132	1.13	0.12673	0.00189	6.32058	0.104	0.36176	0.00468	2053	13	2021	14	1991	22
19A04-58	4	93	0.04	0.15365	0.00239	10.01641	0.17054	0.47287	0.00619	2387	14	2436	16	2496	27
19A04-59	58	64	0.91	0.05663	0.00405	0.42146	0.02954	0.05398	0.00114	477	118	357	21	339	7
19A04-60	2	52	0.04	0.1187	0.0021	5.63597	0.10664	0.3444	0.00463	1937	16	1922	16	1908	22
19A04-61	16	370	0.04	0.29834	0.00355	28.88954	0.40017	0.70236	0.00884	3462	10	3450	14	3430	33
19A04-62	173	154	1.12	0.0541	0.00179	0.41222	0.01371	0.05527	0.0008	375	49	350	10	347	5
19A04-63	112	146	0.76	0.12378	0.00156	6.29961	0.091	0.36913	0.00466	2011	11	2018	13	2025	22
19A04-64	118	61	1.94	0.16397	0.00219	10.60456	0.16025	0.46908	0.00605	2497	11	2489	14	2480	27
19A04-65	137	220	0.62	0.05616	0.00181	0.33932	0.01095	0.04382	0.00063	459	46	297	8	276	4
19A04-66	120	118	1.02	0.16009	0.00202	10.30114	0.14958	0.46669	0.00593	2457	11	2462	13	2469	26

19A04-67	21	24	0.85	0.12536	0.00231	6.46674	0.12662	0.37414	0.0052	2034	17	2041	17	2049	24
19A04-68	35	41	0.84	0.11884	0.00193	5.75902	0.10153	0.35148	0.00469	1939	15	1940	15	1942	22
19A04-69	37	47	0.79	0.05477	0.00207	0.38877	0.01462	0.05148	0.0008	403	56	333	11	324	5
19A04-70	59	30	2.00	0.15374	0.00268	9.38833	0.17592	0.44289	0.00617	2388	15	2377	17	2364	28
19A04-71	7	11	0.69	0.1705	0.00331	11.47115	0.23621	0.48796	0.00716	2563	17	2562	19	2562	31
19A04-72	78	72	1.09	0.0543	0.00296	0.40845	0.02194	0.05455	0.00098	384	88	348	16	342	6
19A04-73	240	342	0.70	0.15176	0.00211	7.67566	0.12042	0.36681	0.00474	2366	12	2194	14	2014	22
19A04-74	22	20	1.09	0.12751	0.00232	6.67742	0.13004	0.37981	0.00526	2064	17	2070	17	2075	25
19A04-75	108	105	1.02	0.1278	0.00187	6.51034	0.1066	0.36947	0.00481	2068	13	2047	14	2027	23
19A04-76	70	68	1.02	0.05483	0.00181	0.38535	0.01281	0.05097	0.00075	405	48	331	9	320	5

*The data marked in red is discordant.

Table S2: whole–rock major and trace element compositions of volcanic rocks

Sample	19A01-1	19A01-2	19A01-3	19A12-1	19A12-2	TLS18-22-1	TLS18-22-2	TLS18-22-3	TLS18-22-4	TLS18-22-5	TLS18-22-6	TLS18-22-7
Rock type	Dacite		Andesite	Rhyolite		Dacite				Andesite		
SiO_2	59.79	63.91	63.80	75.91	73.35	66.42	66.87	65.79	68.37	56.65	56.93	56.78
TiO_2	0.83	0.48	0.65	0.08	0.17	0.36	0.38	0.44	0.35	0.81	0.81	0.83
Al_2O_3	15.54	14.97	15.20	13.02	13.81	15.58	15.33	15.95	15.40	16.48	16.36	16.82
$Fe_2O_3^T$	4.99	3.57	4.30	1.55	2.48	3.87	4.14	4.46	3.70	8.35	7.95	6.11
MnO	0.08	0.07	0.08	0.04	0.06	0.05	0.06	0.06	0.05	0.09	0.09	0.07
MgO	2.05	1.67	2.10	0.03	0.14	1.55	1.60	1.76	1.48	2.80	2.66	2.93
CaO	4.36	2.87	2.09	0.40	0.47	2.69	2.63	2.72	2.25	5.16	5.07	6.08
Na_2O	4.21	5.31	5.12	5.28	4.87	2.22	2.10	2.18	1.96	3.62	3.56	3.46
K_2O	2.70	3.53	3.25	3.18	4.25	3.39	3.15	3.15	3.30	1.12	1.21	2.08
P_2O_5	0.29	0.15	0.22	0.01	0.03	0.12	0.11	0.13	0.11	0.23	0.24	0.24
Total	94.84	96.53	96.81	99.50	99.63	96.25	96.37	96.64	96.97	95.31	94.88	95.40
L.O.I.	4.96	3.16	2.23	0.53	0.54	3.51	3.45	3.51	3.29	4.81	5.03	4.59
σ	2.84	3.74	3.37	2.17	2.74	1.34	1.15	1.25	1.09	1.65	1.63	2.23
A/CNK	0.87	0.84	0.96	1.01	1.02	1.27	1.31	1.33	1.41	0.99	1.00	0.88
A/NK	1.58	1.19	1.27	1.07	1.09	2.13	2.23	2.28	2.26	2.30	2.28	2.12
Trace element (ppm)												
Ba	624	1240	983	229	1370	1200.0	1100.0	1080.0	1090.0	703.0	772.0	881.0
Rb	102.0	102.0	92.7	85.1	114.5	102.00	99.20	98.50	108.5	27.7	28.40	42.40
Sr	427	309	380	30.4	58.9	479.0	432.0	447.0	404.00	669.00	665.0	820.0
Ta	0.6	0.8	0.7	0.9	0.8	0.6	0.6	0.5	0.60	0.50	0.5	0.5
Nb	11.2	11.7	11.5	16.3	15.3	6.80	7.10	7.00	6.80	7.30	7.20	7.60
Hf	6.1	5.9	5.9	6.9	7.5	5.20	5.20	4.90	5.00	4.00	3.90	4.00
Zr	269	253	256	280	337	194.00	197.00	194.00	184.00	151.00	150.00	156.00
Y	26.1	24.7	25.6	36.4	33.1	14.80	14.90	15.1	14.3	19.4	19.0	17.5
Th	11.50	13.15	13.05	16.90	14.35	7.50	7.65	7.25	7.76	4.53	4.46	4.61
U	2.87	3.23	3.16	3.54	3.16	2.4	2.4	2.3	2.3	1.5	1.4	1.5

Cr	20	20	20	<10	<10	90	100	90	90	90	90	130
V	65	55	56	<5	<5	50	69	72	64	163	162	155
Ga	19.9	17.3	19.0	17.7	17.3	18.7	19.3	19.7	19.4	19.7	19.7	20.4
Sr/Y	16.4	12.5	14.8	0.8	1.8	32.4	29.0	29.6	28.3	34.5	35.0	46.9
REE(ppm)												
La	38.1	40.2	41.7	52.9	49.5	30.70	31.30	31.00	30.80	27.70	27.30	27.90
Ce	78.5	82.1	83.2	110.5	102.5	58.5	58.7	59.8	58.00	55.20	54.6	56.6
Pr	8.75	8.85	8.96	12.35	11.25	6.5	6.7	6.7	6.40	6.61	6.6	6.7
Nd	33.4	32.3	33.2	44.3	40.8	22.50	24.00	23.10	22.60	25.70	25.50	25.80
Sm	6.89	6.10	6.82	8.63	8.01	3.73	3.89	3.91	3.75	4.88	4.79	4.65
Eu	1.77	1.54	1.49	0.25	0.92	0.96	1.03	0.97	0.98	1.22	1.28	1.32
Gd	5.60	5.12	5.46	6.59	5.67	3.0	3.1	3.2	3.0	4.4	4.0	4.2
Tb	0.83	0.75	0.83	1.05	0.96	0.44	0.46	0.45	0.44	0.60	0.59	0.62
Dy	4.65	4.25	4.73	6.32	5.64	2.64	2.86	2.69	2.54	3.52	3.55	3.39
Ho	0.94	0.86	0.91	1.35	1.18	0.5	0.6	0.6	0.5	0.7	0.7	0.7
Er	2.65	2.47	2.65	3.89	3.47	1.6	1.6	1.7	1.5	2.0	2.1	1.8
Tm	0.39	0.39	0.41	0.62	0.53	0.24	0.24	0.25	0.24	0.29	0.31	0.27
Yb	2.50	2.50	2.61	3.88	3.29	1.60	1.59	1.65	1.58	1.80	1.88	1.72
Lu	0.39	0.38	0.40	0.64	0.56	0.26	0.25	0.25	0.24	0.27	0.28	0.26
LREE	167.41	171.09	175.3	228.93	212.98	122.89	125.61	125.44	122.53	121.31	120.04	122.94
HREE	17.95	16.72	18	24.34	21.3	10.31	10.67	10.73	10.04	13.57	13.45	12.98
∑REE	185.36	187.81	193.3	253.27	234.28	133.2	136.28	136.17	132.57	134.88	133.49	135.92
LREE/HRE	9.3	10.2	9.7	9.4	10.0	11.9	11.8	11.7	12.2	8.9	8.9	9.5
(La/Yb)N	10.93	11.53	11.46	9.78	10.79	13.76	14.12	13.48	13.98	11.04	10.42	11.64
δEu	0.84	0.82	0.72	0.10	0.40	0.85	0.88	0.81	0.87	0.79	0.87	0.89

Table S3: References of geochronological data in Langshan zone

(1) Teng, X.J., Tian, J., Liu, Y., Zhang, Y., Teng, F., Duan, X.L., 2018. Definition and geological significance of early Silurian quartz diorite pluton in Langshan area, Inner Mongolia. Earth Science, 44, 1236-1252 (in Chinese with English abstract).

(2) Wang, Z.Z., Han, B.F., Feng, L.X., Liu, B., 2015. Geochronology, geochemistry and origins of the Paleozoic–Triassic plutons in the Langshan area, western Inner Mongolia, China. Journal of Asian Earth Sciences 97 (Part B, no. 0), 337–351.

(3) Liu, Y., Wang, W. L., Teng, X. J., Guo, S., Teng, F., He, P., Tian, J., Duan, X. L., 2019. Geochemistry and Hf isotopes characteristics and geological significance of latest early Permian granodiorite of Langshan area，Inner Mongolia. Advances in Earth Science，34（4）：366-381. DOI：10. 11867/j. issn. 1001-8166. 2019. 04. 0366 (in Chinese with English abstract).

(4) Wang, W. L., Teng, X. J., Liu, Y., Teng, F., Guo, S., He, P., Tian, J., Duan, X. L., 2018. Geochemical characteristic, LA-ICP-MS zircon U-Pb dating and Hf isotopic compositions of the Haorigeshan monzogranite in the Langshan Region, Inner Mongolia. Acta Geologica Sinica 92(11):2227-2247 (in Chinese with English abstract).

(6) Dan, W., Li, X.H., Wang, Q., Wang, X.C., Wyman, D.A., Liu, Y., 2016. Phanerozoic amalgamation of the Alxa Block and North China Craton: evidence from Paleozoic granitoids, U–Pb geochronology and Sr–Nd–Pb–Hf–O isotope geochemistry. Gondwana Research, 32:105-121 http://dx.doi.org/10.1016/j.gr.2015.02.011

(7) Shi, X. J., Tong, Y., Wang, T., Zhang, J. J., Zhang, Z. C., Zhang, L., Guo, L., Zeng, T. Geng, J. Z. (2012). LA-ICP-MS zircon U–Pb age and geochemistry of the Early Permian Halinudeng granite in northern Alxa area, western Inner Mongolia. Geological Bulletin of China 31, 662–670 (in Chinese with English abstract).

(8) Geng, Y. S., Zhou, X. W., 2012. Early Permian magmatic events in the Alxa metamorphic basement: Evidence from geochronology. Acta Petrologica Sinica 28(9), 2667–2685 (in Chinese with English abstract).

(9) Li, J.J., 2006. Regional Metallogenic System of Alashan Block in Inner Mongolia. Dissertation for the Doctoral Degree. China University of Geosciences, Beijing, p. 11 (in Chinese).

(10) Feng, J. Y., Xiao, W. J., Windley, B. F., Han, C. M., Wan, B., Zhang, J. E., Ao, S.J., Zhang, Z.Y., Lin, L.N., 2013. Field geology, geochronology and geochemistry of mafic–ultramafic rocks from Alxa, China: Implications for Late Permian accretionary tectonics in the southern Altaids. Journal of Asian Earth Sciences 78, 114–142.

(11) Zhang, J. J., Wang, T., Castro, A., Zhang, L., Shi, X. J., Tong, Y., Zhang, Z.C., Guo, L., Yang, Q.D., Maria Iaccheri, L., 2016. Multiple mixing and hybridization from magma source to final emplacement in the Permian Yamatu pluton, the northern Alxa block, China. Journal of Petrology 57(5), 933–980.

Supplementary figure: Cumulative probability curves of measured crystallization ages for detrital zircons grains relative to the depositional age of samples from the Permian Dahongshan Formation (19A03 and 19A04).

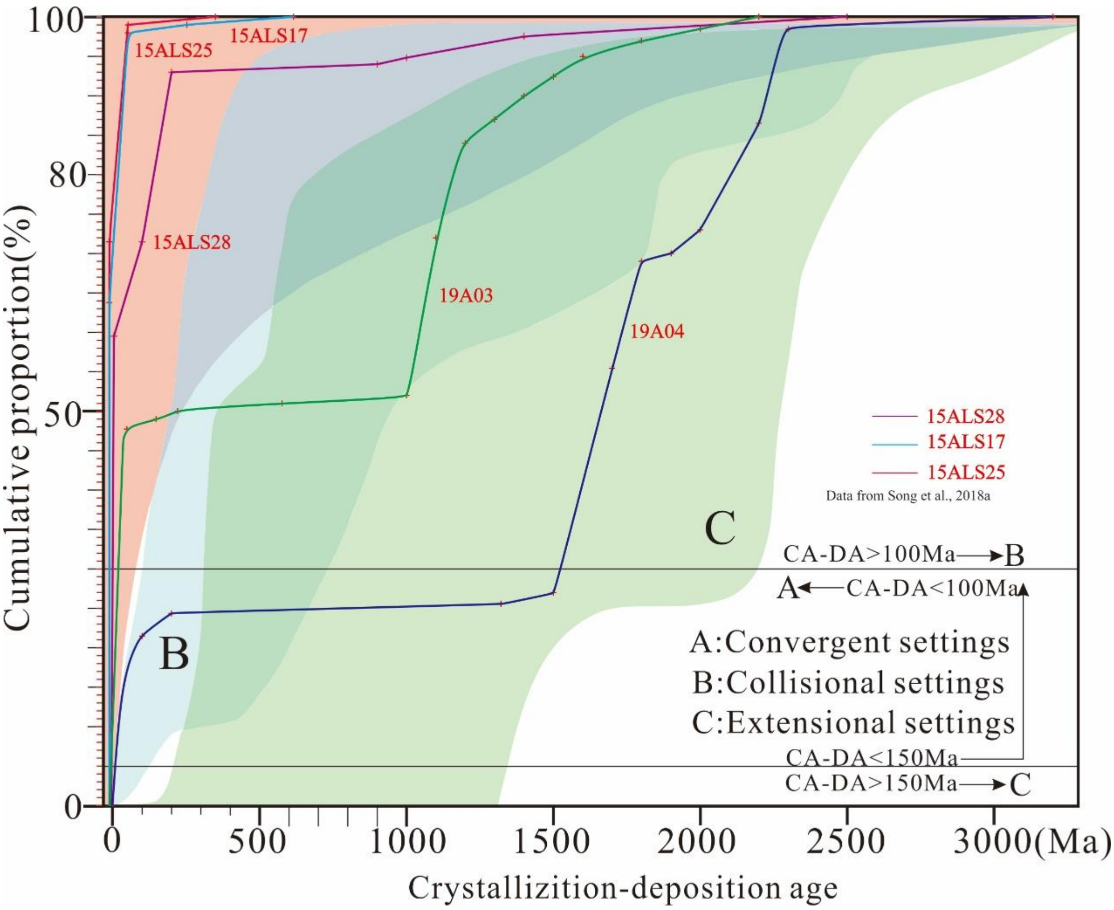

We use 265 Ma as the depositional age of the Permian strata in Langshan (adjacent to our study region) based on the zircon U–Pb ages of the interlayer volcanic rocks (Guo et al., 2017). Two samples from the Dahongshan Formation plot into the convergent setting (19A03) and collisional setting (19A04). Associating with the detrital zircon age spectrum, lithology and terrestrial plant fossils in this Formation, we argue that the Dahongshan Formation was most likely deposited in a retroarc foreland basin. The Permian samples from the western Alxa Block (Song et al., 2018a) plot into the convergent setting, probably in a forearc basin.

References

Guo, S., Teng, X.J., Liu, Y., Teng, F., He, P., Wang, W.L., Tian, J., Duan, X.L., 2017. Geochemistry, chronology and Hf isotope features of the Permian intermediate–basic volcanic rocks in Wulanaobao area, Urad Houqi, Inner Mongolia and its geological significance. Journal of Geomechanics, 23:397–410 (in Chinese with English abstract).

Song, D., Xiao, W., Collins, A.S., Glorie, S., Han, C., Li, Y., 2018a. Final Subduction Processes of the Paleo–Asian Ocean in the Alxa Tectonic Belt (NW China): Constraints from Field and Chronological Data of Permian Arc–Related Volcano–Sedimentary Rocks. Tectonic 37, 1658–1687.